Perturbative quantum Monte Carlo study of $LiHoF_4$ in a transverse magnetic field

S. M. A. Tabei,[1] M. J. P. Gingras,[1,2] Y.-J. Kao,[3] and T. Yavors'kii[1]
[1]*Department of Physics and Astronomy, University of Waterloo, Waterloo, Ontario, Canada N2L 3G1*
[2]*Canadian Institute for Advanced Research, 180 Dundas Street West, Toronto, Ontario, Canada M5G 1Z8*
[3]*Department of Physics and Center for Theoretical Sciences, National Taiwan University, Taipei 10617, Taiwan*
(Received 21 December 2007; revised manuscript received 16 July 2008; published 11 November 2008)

Results from a recent quantum Monte Carlo (QMC) study [P. B. Chakraborty *et al.*, Phys. Rev. B **70**, 144411 (2004)] of a model of the $LiHoF_4$ Ising magnetic material in an external transverse magnetic field, B_x, show a discrepancy with experimental results, even for small B_x where quantum fluctuations are small. This discrepancy persists asymptotically close to the classical ferromagnet to paramagnet phase transition. In this paper, we numerically reinvestigate the temperature T versus transverse-field phase diagram of $LiHoF_4$ in the regime of weak B_x. In this regime, starting from an effective low-energy spin-1/2 description of $LiHoF_4$, we apply a cumulant expansion to derive an effective temperature-dependent classical Hamiltonian that incorporates perturbatively the small quantum fluctuations in the vicinity of the classical phase transition at $B_x=0$. Via this effective classical Hamiltonian, we study the B_x-T phase diagram via classical Monte Carlo simulations. In particular, we investigate the influence on the phase diagram of various effects that may be at the source of the discrepancy between the previous QMC results and the experimental ones. In particular, we consider two different ways of handling the long-range dipole-dipole interactions and explore how the B_x-T phase diagram is modified when using different microscopic crystal-field Hamiltonians. The main conclusion of our work is that we fully reproduce the previous QMC results at small B_x. Unfortunately, none of the modifications to the microscopic Hamiltonian that we explore are able to provide a B_x-T phase diagram compatible with the experiments in the quasiclassical small B_x regime.

DOI: 10.1103/PhysRevB.78.184408 PACS number(s): 75.10.Jm, 75.40.Mg, 75.30.Kz

I. INTRODUCTION

A. Transverse-field Ising model

Phase transitions from order to disorder are most commonly driven by thermal fluctuations. However, near absolute zero temperature, a system can, via *quantum* fluctuations associated with the Heisenberg uncertainty principle, undergo a quantum phase transition (QPT).[1,2] The transverse-field Ising model (TFIM) is perhaps the simplest model that exhibits a QPT.[1,3,4] This model was first proposed by de Gennes to describe proton tunneling in ferroelectric systems.[5] The Hamiltonian of the TFIM is given by

$$H_{\mathrm{TFIM}} = -\frac{1}{2}\sum_{i,j} J_{ij}\sigma_i^z\sigma_j^z - \Gamma\sum_i \sigma_i^x, \tag{1}$$

where σ_i^μ ($\mu=x,y,z$) are the Pauli matrices. Since σ_i^x and σ_i^z do not commute, a nonzero field, Γ, transverse to the Ising direction, causes quantum tunneling between the spin-up and spin-down eigenstates of σ_i^z, hence causing quantum spin fluctuations. These fluctuations decrease the critical temperature T_c at which the spins develop long-range order. In the simplest scenario, where $J_{ij}>0$, the ordered phase is ferromagnetic.[3,4] At a critical field Γ_c, T_c vanishes, and a quantum phase transition between a long-range-ordered ferromagnetic phase and a quantum paramagnet (PM) state occurs. The H_{TFIM} can be generalized by considering J_{ij} as quenched (frozen) random interactions. Competing ferromagnetic $J_{ij}>0$ and antiferromagnetic $J_{ij}<0$ couplings generate random frustration. For a three-dimensional case, the system freezes into an (Ising) spin-glass state at a critical temperature T_g.[6,7] Similar to the previous example, $T_g(\Gamma)$ decreases as Γ is increased until, at $\Gamma=\Gamma_c$, a quantum phase transition between a spin-glass phase and a PM state occurs. Extensive numerical studies have found the QPT between a quantum paramagnet and a spin-glass phase[8–10] to be quite interesting due to the occurrence of Griffiths-McCoy singularities (GMSs).[11,12]

B. $LiHo_xY_{1-x}F_4$

The magnetic insulator $LiHoF_4$, with a magnetic field B_x applied perpendicular to the Ising z direction of the Ho^{3+} magnetic moments, is a well-known example of a physical realization of the transverse-field Ising model.[13–16] The predominant J_{ij} interactions between the Ho^{3+} ions in $LiHoF_4$ are long-range magnetostatic dipole-dipole interactions which decay as $1/r_{ij}^3$, where r_{ij} is the distance between the i and j ions. The sign of J_{ij} depends on the position of j with respect to i. The existence of a large crystal-field anisotropy on the magnetic Ho^{3+} ions[17] causes the system to behave as a classical Ising system with dipolar interactions for $B_x=0$. The reason is that the single-ion crystal-field ground state is an Ising doublet, meaning that the matrix elements of the raising and lowering angular momentum operators $J^{\pm}$ vanish within the space spanned by the two states of the doublet. The Ising direction is parallel to the **c** axis of the body-centered-tetragonal structure of $LiHoF_4$. For $B_x=0$, the system is well described by a low-energy effective spin-1/2 classical dipolar Ising model.[18–20] Because the energy gap between the ground doublet and the first excited singlet is fairly large compared to the J_{ij} couplings, there is little quantum-mechanical admixing between the ground doublet and the excited state induced by the interactions.[18] However,

a nonzero B_x admixes the ground doublet with the excited singlet and splits the ground doublet. It is this energy splitting which corresponds to the effective transverse field Γ in the TFIM description of $LiHoF_4$ in nonzero B_x.[13,19,20]

The Ho^{3+} ions may be substituted (i.e., randomly diluted) by nonmagnetic yttrium (Y^{3+}) ions, with very little lattice distortion. This allows one to study the effects of disorder on $LiHo_xY_{1-x}F_4$ as an example of a diluted Ising model. Depending on the concentration x of magnetic ions, the low-temperature phase is either ferromagnetic[13,21] or spin glass.[22–26] Interestingly, paradoxical phenomena are observed when a transverse magnetic field is applied to $LiHo_xY_{1-x}F_4$, with $x<1$. In the ferromagnetic regime, $(0.25<x<1.0)$, when $B_x=0$, a mean-field behavior $T_c(x)\propto x$ for the paramagnet to ferromagnet temperature transition is observed. However, in nonzero B_x, with increasing B_x, $T_c(B_x)$ decreases faster than mean-field theory predicts.[27] For $B_x=0$, when $LiHo_xY_{1-x}F_4$ is diluted below $x\approx 0.25$, a conventional spin-glass transition is observed.[14,23–26] A signature of a spin-glass transition is the divergence of the nonlinear magnetic susceptibility at T_g.[28] However, surprisingly, $\chi_3(T)$ in $LiHo_xY_{1-x}F_4$ becomes less singular as B_x is increased from $B_x=0$, suggesting that no quantum phase transition between a PM and a spin-glass (SG) state exists as $T\rightarrow 0$.[14,29] Recently, theoretical studies[19,30–32] have suggested that for dipole-coupled Ho^{3+} in diluted $LiHo_xY_{1-x}F_4$, nonzero B_x generates longitudinal (along the Ising $\hat{z}$ direction) random fields that couple to the magnetic moment. These random fields (i) lead to a faster decrease of $T_c(B_x)$ in the ferromagnetic regime and (ii) destroy the paramagnet to spin glass transition in $LiHo_xY_{1-x}F_4$ samples that otherwise show a SG transition when $B_x=0$.[23–26] The influence of these induced random fields on the behavior of the linear magnetic susceptibility χ in nonzero B_x has recently been investigated for ferromagnetic $LiHo_xY_{1-x}F_4$ samples.[21] When $LiHo_xY_{1-x}F_4$ is highly diluted (e.g., $LiHo_{0.045}Y_{0.955}F_4$), a very interesting and peculiar behavior is observed. ac susceptibility data show that the distribution of relaxation times *narrows* upon cooling below 300 mK.[22,26,33,34] This behavior is quite different from that observed in conventional spin glasses, where the distribution of relaxation times broadens upon approaching a spin-glass transition at $T_g>0$.[6,28] This so-called *antiglass* behavior has been interpreted as evidence that the spin-glass transition in $LiHo_xY_{1-x}F_4$ disappears at some nonzero $x_c>0$.[23,24] This is in contrast with theoretical arguments,[35] which reason that because of the long-ranged $1/r^3$ nature of dipolar interactions, classical dipolar Ising spin glasses should have $T_g(x)>0$ for all $x>0$. However, recent numerical[36–38] and experimental works[23,24] claimed that a finite temperature paramagnetic to spin glass phase transition may not occur for x as large as $x_c\approx 0.2$. The experimental[26,39] and numerical[40] situations remain unsettled and in a rapid state of change.

C. $LiHoF_4$ as a TFIM

In addition to the phenomena arising in the diluted regime of $LiHo_xY_{1-x}F_4$, the $x=1$ regime also turns out to be interesting. There still exist problems for pure $LiHoF_4$ which require the properties of this system in nonzero B_x to be reinvestigated more thoroughly. The properties of $LiHoF_4$ in a transverse external magnetic field have only recently been studied in quantitative detail starting from a truly microscopic spin Hamiltonian.[20] In Ref. 20, which reported results from a quantum Monte Carlo (QMC) study using the stochastic series-expansion (SSE) technique,[41] general qualitative agreement between the microscopic model and experimental data[13] was obtained. However, as illustrated in Fig. 1, there is significant quantitative discrepancy between the Monte Carlo results of Ref. 20 and the experimental data of Ref. 13. In particular, the discrepancy between experimental results and QMC results persists asymptotically close to the classical ferromagnetic to paramagnetic phase transition, where B_x/T_c and quantum fluctuations are *perturbatively small*. For very low temperatures and high B_x, it is crucial to consider the hyperfine interaction in order to explain the behavior of the phase diagram close to the quantum critical point.[13,20,42] For very small B_x/T_c, the numerical results shown in the inset of Fig. 1 indicate that the effect of the hyperfine interaction is not important close to the classical transition at $T_c\approx 1.53$ K.

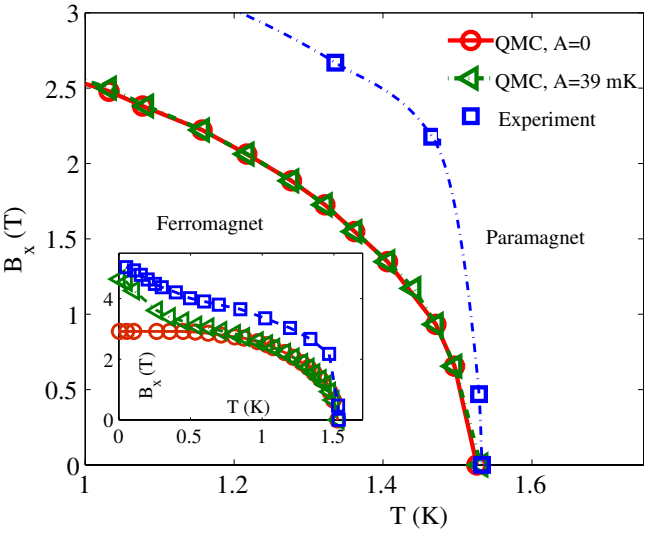

FIG. 1. (Color online) The discrepancy between the experimental (Ref. 13) phase diagram of $LiHoF_4$ and QMC simulations using stochastic series expansion for small B_x from Ref. 20. The whole phase diagram is shown in the inset. At low temperature and high B_x, neglecting the large hyperfine interaction A generates a large discrepancy between the experimental quantum critical point and the one obtained from simulation. However, at low B_x and close to the classical critical point, the hyperfine interaction is not a quantitatively important parameter. Other possibilities for the origin of this discrepancy have to be investigated in this regime.

It was suggested in Ref. 20 that the discrepancy between simulation and experiment, close to the classical transition, may be related to some uncertainty in the crystal-field parameters (CFPs) used in the crystal-field Hamiltonian which enters in the TFIM description of $LiHoF_4$ and which is simulated via QMC. Indeed, a number of CFP sets obtained from different experimental works, such as susceptibility measurements,[17] neutron scattering,[16] and electron-paramagnetic-resonance experiments,[43] provide somewhat different values for the CFPs. The important point here is

that different CFPs would lead to different field (B_x)–dependent effective coupling parameters in the TFIM description of $LiHoF_4$, which would result in different B_x vs T_c phase diagrams.

Yet, there are other factors of strictly computational nature which may be at the origin of the discrepancy illustrated in Fig. 1. In particular, calculations that involve long-range dipolar interactions are notoriously tricky to handle. Because of the long-range nature and angular dependence of dipolar interactions, the dipolar sum $U(i)=1/N\Sigma_j(1-3\cos^2\theta_{ij})/r_{ij}^3$ is conditionally convergent.[44–46] That is, the value of the sum depends on the shape of the external boundary of the system studied. Here, r_{ij} is the distance between sites i and j and θ_{ij} is the angle between r_{ij} and the global Ising $\hat{z}$ spin axis. For example, the conditional convergence of dipolar sums was studied by Luttinger and Tisza,[46] who performed the dipolar sums for a number of spin structures for systems with different external boundary shapes. For example, they considered an infinitely large system of dipoles on a body-centered-cubic lattice. They found that when the external boundary is spherical, the ground state is antiferromagnetic, while it is ferromagnetic for a needle-shaped sample. Later, Griffiths[47] rigorously proved that for zero external field, the free energy for a dipolar lattice system has to be independent of the sample shape in the thermodynamic limit. The immediate consequence of Griffiths' theorem is that in zero external field, the net magnetization of the sample has to be zero. Otherwise, the field originating from the magnetic moments sitting on the boundary of the sample would couple to the dipolar moments of the sample, making the free energy shape dependent. Therefore, according to Griffiths' theorem,[47] domains are formed in the sample such that in the thermodynamic limit, the total magnetization is zero. Griffiths' theorem contradicts the results of Luttinger and Tisza.[46] The reason is that Luttinger and Tisza assumed a uniform ground-state spin configuration and ignored the possibility of domain formation. This discussion emphasizes the complication of studying systems with dipolar interactions and the caution which should be taken while dealing with such systems (e.g., the choice of the boundary geometry, boundary conditions, and the shape of the domain walls). Finite-size effects are another issue that needs to be handled quite carefully in systems where there are long-range interactions between ions.

There are different ways to incorporate dipolar interactions in a computationally efficient way. Reference 20 implemented the reaction-field method,[48] which truncates the sum of the long-range interactions at the boundary of a sphere. The dipoles outside the sphere are treated in a mean-field fashion. Due to the semi-mean-field nature of this method, the reaction-field method overestimates the critical temperature. In the presence of quantum fluctuations, this overestimation is still at play and can possibly influence the B_x-T_c phase diagram as well. The Ewald summation method[44,49–53] is another method used to treat the long-range dipolar interactions. In the Ewald summation method, a specified volume is periodically replicated. Then, by summing instead two convergent series effectively representing the dipolar interactions between magnetic moments i and j and all the periodically repeated images of j, an effective dipole-dipole interaction between two arbitrary magnetic moments i and j within the finite-size sample to be numerically simulated is derived. From a general perspective, it would appear quite worthwhile to investigate the applicability and usefulness of the Ewald summation method to determine the low B_x vs T_c phase diagram of $LiHoF_4$. Indeed, the Ewald summation method, unlike the reaction-field one, is less prone to mean-field overestimations and can be used as another methodology to probe the $LiHoF_4$ problem via simulations.[37,38]

Another factor whose influence on the B_x-T phase diagram should be studied is the nearest-neighbor exchange interaction J_{ex} in $LiHoF_4$. The strength of J_{ex}, which is expected to be comparable to the dipolar interactions for a $4f$ ion, such as Ho^{3+}, is unknown. The strength can be determined such that the classical critical temperature matches the experimental value for $B_x=0$. The estimated value of J_{ex} is highly sensitive to the method used to handle the external boundaries and finite-size effects in simulations, both of which have significant effects when the reaction-field (RF) method is used, as already found in Ref. 20.

D. Scope of the paper

The above discussion should make it clear that there are two rather distinct avenues to pursue in order to seek an explanation for the discrepancy illustrated in Fig. 1 between the experimental[13] B_x vs T_c phase diagram of $LiHoF_4$ and the one obtained via QMC.[20] One avenue is that the current microscopic model is incomplete. As mentioned above and suggested in Ref. 20, one possible source for this incompleteness may be an inaccurate set of CFPs. Another possible source is that interactions other than long-range magnetic dipolar interactions and nearest-neighbor exchange may be at play.[54] Examples of other interactions include higher-order multipole interactions and virtual-phonon exchange.[54] The other avenue is related to the ensemble of computational pitfalls and ensuing numerical errors that may arise when one deals with long-range dipolar interactions through simulations. Therefore, before one delves into exploring a more complex microscopic Hamiltonian, there is a clear need to reinvestigate the "simpler" problem that solely considers long-range dipole-dipole interactions and nearest-neighbor exchange.

In this work we aim to scrutinize the individual role of each of the computational issues as a potential culprit for the discrepancy observed in Fig. 1. Because QMC and experiment do not match at $B_x/T_c \to 0$, we have developed a tool that allows us to achieve the goal in an efficient and computationally simple way. Since the discrepancy appears at low B_x near the classical T_c, where quantum fluctuations within a classical are *perturbatively* small, we can expand the partition function Z in terms of the transverse magnetic field B_x and recast the partition function as a sum over strictly classical states by using an effective *classical* Hamiltonian $H_{\text{eff}}(T)$. In $H_{\text{eff}}(T)$, the quantum effects are incorporated perturbatively, giving us the ability to calculate all thermodynamical quantities in the presence of small quantum fluctuations within a classical Monte Carlo method. Therefore, a classical Monte Carlo simulations can be performed using

$H_{\text{eff}}(T)$ in a very simple way, without the need to perform complicated QMC (Refs. 20 and 41) simulations when considering a regime with weak quantum fluctuations.[55] Therefore, we can focus on the region close to the classical transition and investigate the different possible origins of the discrepancy in detail.

In summary, (i) the complexity of the QMC SSE method, (ii) the problematic conditional convergence of dipolar lattice sums, (iii) the question of controlled finite-size effects and its role on a consistent determination of the nearest-neighbor exchange J_{ex}, and (iv) the possible sensitivity of the $T_c(B_x)$ dependence on the choice of CFPs altogether warrant a new numerical investigation of the $T_c(B_x)$ phase diagram in the $LiHoF_4$ transverse-field Ising material. Below, we will show that either fortunately or unfortunately, depending on one's disposition, the factors proposed in Sec. I C as the possible origins of the discrepancy between experiment and simulation (see Fig. 1) are apparently not the issue. Therefore, the origin of the discrepancy remains unexplained. However, the perturbative cumulant Monte Carlo tool that we have devised could be used effectively to search for the cause of discrepancy. Without it, the discovery of the irrelevance of the above factors through classical Monte Carlo simulation would have been a more CPU time consuming burden. Ultimately, the same tool can also be used to explore the role of the small B_x when $x \neq 0$.[21,30–32] Indeed, constructing the whole x-$T_c(B_x)$ phase diagram in the "small B_x" in the vicinity of the classical x-T_c phase diagram by performing solely classical Monte Carlo was an original key motivation for the development of the method presented in this paper.

The rest of the paper is organized as follows: In Sec. II, we review the crystal structure and the physical properties of $LiHoF_4$ in a transverse field B_x and the effect of the choice of crystal-field potential on the magnetic low-energy states. In Sec. III, we introduce the full microscopic Hamiltonian of $LiHoF_4$. We discuss how for low energies, an effective spin-1/2 Hamiltonian for $LiHoF_4$ can be constructed, and we explain how one can picture $LiHoF_4$ in nonzero B_x as a dipolar TFIM. We then discuss how a semiclassical effective Hamiltonian is derived from the TFIM Hamiltonian by incorporating the transverse-field term perturbatively via a cumulant expansion. In Sec. IV, we employ the semiclassical effective Hamiltonian obtained in Sec. III in classical Monte Carlo simulations for small B_x. We discuss the results obtained using either the reaction-field or the Ewald summation method. We discuss how the nearest-neighbor exchange J_{ex} is estimated and we investigate the sensitivity of the determined J_{ex} value upon the choice of the numerical method. Finally, we compare the B_x-T_c phase diagrams originating from two different sets of crystal-field parameters. Section V summarizes our results.

II. STRUCTURE AND CRYSTAL FIELD

The magnetic material $LiHoF_4$ undergoes a second-order phase transition from a paramagnetic to a ferromagnetic state at a critical temperature of 1.53 K.[14,17] The critical temperature can be reduced by applying a magnetic field B_x transverse to the Ising easy-axis direction. The magnetic field induces quantum fluctuations such that beyond a critical field of $B_x^c \approx 4.9$ T, the system displays a quantum phase transition from a ferromagnetic state to a quantum paramagnetic state at zero temperature.[13,15,16] The magnetic properties of $LiHoF_4$ are due to Ho^{3+} rare-earth magnetic ions. The electronic ground state of Ho^{3+} is $4f^{10}$, which gives small exchange coupling,[20,56,57] such that the predominant magnetic interaction between the Ho^{3+} ions are long-range magnetic dipole-dipole interactions. Hund's rules dictate that the total angular momentum of a free ion Ho^{3+} is J=8 (L=6 and S=2) and the electronic ground-state configuration is $^5I_8$. $LiHoF_4$ is a compound with space group $C_{4h}^6(I4_1/a)$ and lattice parameters $a=b=5.175$ Å and $c=10.75$ Å. It has four Ho^{3+} ions per unit cell positioned at (0,0,1/2,), (0,1/2,3/4), (1/2,1/2,0), and (1/2,01/4).[56] The crystal has S_4 symmetry, which means the lattice is invariant with respect to a $\frac{\pi}{2}$ rotation about the z axis and reflection with respect to the x-y plane.

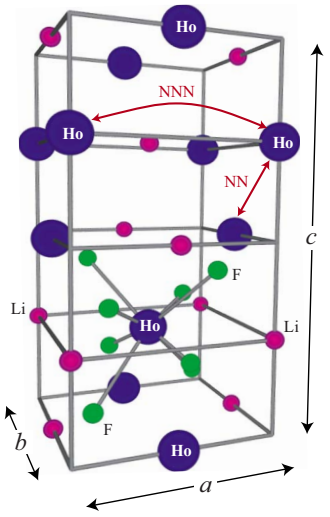

$a = b = 5.176$ Å

$c = 10.75$ Å

FIG. 2. (Color online) The crystal structure of $LiHoF_4$. NN identifies the first-nearest neighbors and NNN identifies the next-nearest neighbors.

In the crystal structure (Fig. 2), the Ho^{3+} ions are surrounded by F^- ions, which create a strong crystal electric field with S_4 symmetry. This crystal field lifts the 17-fold degeneracy of the $^5I_8$ configuration, giving a non-Kramers ground-state doublet. The next excited state is a singlet with an energy gap of ≈ 11 K above the ground-state doublet.[16,17,43,58] The crystal-field Hamiltonian and the crystal-field parametrization are discussed in detail in Appendix A. Holmium is an isotopically pure element with nuclear spin $I=7/2$, which is coupled to the electronic spin $\mathbf{J}$ via the hyperfine contact interaction $A\mathbf{I}\cdot\mathbf{J}$, where $A \approx 39$ mK.[56,59]

III. EFFECTIVE THEORY OF $LiHoF_4$ FOR THE LOW B_x/T_c REGIME

In this section we derive an effective model suitable for describing $LiHoF_4$ in the small-transverse-magnetic-field re-

gime, where $B_x/T_c \to 0$ (T_c is the critical temperature when $B_x=0$). The simplicity gained by using an effective theory gives us the ability to capture the essential physics and to easily reinvestigate the influence of the different parameters affecting the behavior of the phase diagram of $LiHoF_4$ in the $B_x/T_c \to 0$ regime. We derive the required effective model in two steps. First, in $LiHoF_4$, in the temperature range that we are interested in, which is close to or below $T_c(B_x=0)=1.53$ K, the high-energy scales are well separated from the low-energy sector. The energy scale for dipolar interactions between nearest-neighbor Ho^{3+} ions is about 0.31 K. This is much smaller than the energy gap between the two first lowest single-ion energy states and the next-higher crystal-field states (>11 K). In this case, one can neglect the higher-energy states and reduce the full Hamiltonian Hilbert space to a smaller subspace spanned by the two lowest-energy states. This enables us to deduce a low-energy effective spin-1/2 Hamiltonian for $LiHoF_4$. Second, we derive a semiclassical effective Hamiltonian from the low-energy spin-1/2 Hamiltonian by incorporating the transverse-field term perturbatively via a cumulant expansion. We can then perform a classical Monte Carlo using this semiclassical effective Hamiltonian to investigate the small B_x/T_c regime.

A. Effective spin-1/2 Hamiltonian

As mentioned in Sec. II, there are three types of interactions that play a role in the magnetic properties of $LiHoF_4$. The main interaction is the long-range dipole-dipole interaction between the Ho^{3+} magnetic ions denoted by

$$H_{\mathrm{dip}} = \frac{1}{2}(g_L\mu_B)^2 \sum_{i\neq j} \sum_{\mu\nu} L_{ij}^{\mu\nu} \mathrm{J}_i^\mu \mathrm{J}_j^\nu, \tag{2}$$

where $\mu,\nu=x,y,z$ and $\mathbf{J}_i$ is the total angular momentum of Ho^{3+} ion i. $L_{ij}^{\mu\nu}$ is the magnetic dipole interaction, written in the form $L_{ij}^{\mu\nu}(\mathbf{r}_{ij})=(\delta^{\mu\nu}|\mathbf{r}_{ij}|^2-3r_{ij}^\mu \mathbf{r}_{ij}^\nu)/|\mathbf{r}_{ij}|^5$, where $\mathbf{r}_{ij}=\mathbf{r}_j-\mathbf{r}_i$, where $\mathbf{r}_i$ and $\mathbf{r}_j$ are the positions of ions i and j, respectively. $g_L=5/4$ is the Landé g factor of free Ho^{3+} and $\mu_B=0.6717$ K/T is the Bohr magneton. The dipolar interaction is complemented by a short-range nearest-neighbor Heisenberg exchange interaction,

$$H_{\mathrm{exch}} = \frac{1}{2} J_{\mathrm{ex}} \sum_{i,\mathrm{NN}} \mathbf{J}_i \cdot \mathbf{J}_{\mathrm{NN}}, \tag{3}$$

where NN denotes the nearest neighbors of site i. This exchange interaction is considered to be weak and isotropic.[20,60] The third interaction is the hyperfine coupling between the electronic and nuclear magnetic moments,

$$H_{\mathrm{hyp}} = A \sum_i (\mathbf{I}_i \cdot \mathbf{J}_i). \tag{4}$$

The hyperfine constant $A \approx 39$ mK is anomalously large in Ho^{3+}-based materials.[13,20,42] Thus, the complete Hamiltonian is written as

$$H = \sum_i V_C(\mathbf{J}_i) - g_L\mu_B \sum_i B_x \mathrm{J}_i^x + H_{\mathrm{dip}} + H_{\mathrm{exch}} + H_{\mathrm{hyp}}. \tag{5}$$

The first two terms are single-ion interactions, where V_C describes the strong crystal-field interactions discussed in Sec. II and Appendix A. The second term is the Zeeman interaction. Henceforth, we ignore H_{hyp} since our goal, as explained in Sec. I, is to investigate the small B_x and small $[T_c(0)-T_c(B_x)]/T_c(0)$ regime, where, as already suggested by the results of Ref. 20 and, as shown in the inset of Fig. 1, the effects of hyperfine interactions are negligible. The first two single-site (noninteracting) terms in H, denoted as

$$H_{\text{single-site}} = V_C(\mathbf{J}) - g_L\mu_B B_x \mathrm{J}^x, \tag{6}$$

can be easily numerically diagonalized for arbitrary transverse field B_x.[20] $|\alpha(B_x)\rangle$ and $|\beta(B_x)\rangle$ are the two lowest states of the single-ion Hamiltonian [Eq. (6)] for a given B_x. Their corresponding energies are denoted by $E_\alpha(B_x)$ and $E_\beta(B_x)$.

At $B_x=0$ these two states form a doublet, but $B_x \neq 0$ lifts the degeneracy. The Ising subspaces $|\uparrow\rangle$ and $|\downarrow\rangle$ are chosen by performing a unitary rotation on the $|\alpha(B_x)\rangle$ and $|\beta(B_x)\rangle$ states:

$$|\uparrow\rangle = \frac{1}{\sqrt{2}}[|\alpha\rangle + \exp(i\theta)|\beta\rangle],$$

$$|\downarrow\rangle = \frac{1}{\sqrt{2}}[|\alpha\rangle - \exp(i\theta)|\beta\rangle]. \tag{7}$$

The phase θ is chosen such that the matrix elements of the operator J^z between $|\uparrow\rangle$ and $|\downarrow\rangle$ is real and diagonal, giving for J_i^z, $\mathrm{J}_i^z = C_{zz}\sigma_i^z$. Since the first excited state, $|\gamma(B_x)\rangle$, above $|\alpha(B_x)\rangle$ and $|\beta(B_x)\rangle$, is at an energy at least seven times higher than $k_B T_c(B_x)$ and is repelled for all B_x from the $|\alpha(B_x)\rangle$ and $|\beta(B_x)\rangle$ set (see Fig. 1 of Ref. 20), we henceforth neglect all excited crystal-field states and work with a reduced Hilbert space spanned by $|\alpha(B_x)\rangle$ and $|\beta(B_x)\rangle$ or equivalently $|\uparrow\rangle$ and $|\downarrow\rangle$. Projecting the single-ion Hamiltonian in Eq. (6) in this two-dimensional subspace for an arbitrary ion i, we get for the transverse field part of the Hamiltonian

$$H_T = \bar{E}(B_x) - \frac{1}{2}\Delta(B_x)\sigma^x, \tag{8}$$

where $\bar{E}(B_x)=\frac{1}{2}[E_\alpha(B_x)+E_\beta(B_x)]$ and $\Delta(B_x)=E_\beta(B_x)-E_\alpha(B_x)$. The energy difference between the two lowest states induced by the transverse magnetic field B_x can already be interpreted as an effective transverse field $\Gamma=\frac{\Delta(B_x)}{2}$ acting on $S_{\mathrm{eff}}=\frac{1}{2}$ degrees of freedom at each site. The dependence of $\Delta(B_x)$ on the magnetic transverse field B_x is plotted in Fig. 3.

Since we are working with a two-dimensional subspace for each ion i, we can write the interactions between J_i^μ and J_j^ν in terms of interactions between Pauli matrices. Indeed, any operator in a two-dimensional space can be written as a linear combination of σ_i^μ Pauli matrices plus the unit matrix $\sigma^0 \equiv \mathbb{1}$. In order to express J_i^μ in terms of σ_i^μ, we project J_i^μ in the subspace spanned by $|\uparrow\rangle$ and $|\downarrow\rangle$.

Specifically, we write the J^μ operator as

$$\mathrm{J}^\mu = C_{\mu 0}\sigma^0 + \sum_{\nu=x,y,z} C_{\mu\nu}(B_x)\sigma^\nu, \tag{9}$$

where

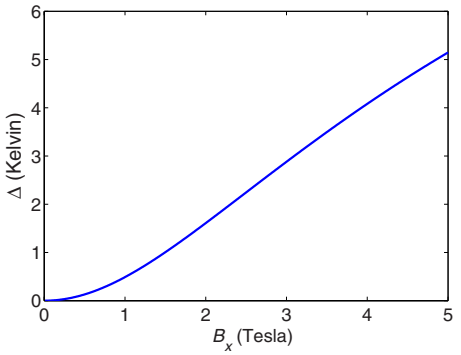

FIG. 3. (Color online) The energy splitting of the ground-state doublet, $\Delta(B_x) \equiv E_\beta(B_x) - E_\alpha(B_x)$, in $LiHoF_4$ as a function of B_x, the transverse magnetic field. The crystal-field V_c was obtained from Refs. 16 and 20. For more details on the crystal field and crystal-field parametrization, refer to Appendix A.

$$C_{\mu 0} = \frac{1}{2}[\langle\uparrow|J^\mu|\uparrow\rangle + \langle\downarrow|J^\mu|\downarrow\rangle],$$

$$C_{\mu z} = \frac{1}{2}[\langle\uparrow|J^\mu|\uparrow\rangle - \langle\downarrow|J^\mu|\downarrow\rangle],$$

and

$$C_{\mu x} = \frac{1}{2}[\langle\uparrow|J^\mu|\downarrow\rangle + \langle\downarrow|J^\mu|\uparrow\rangle],$$

$$C_{\mu y} = \frac{1}{2i}[\langle\uparrow|J^\mu|\downarrow\rangle - \langle\downarrow|J^\mu|\uparrow\rangle].$$

Using the crystal-field parameters of Refs. 16 and 20, the evolution of the $C_{\mu\nu}$ and $C_{\mu 0}$ parameters as a function of B_x is determined and plotted in Fig. 4. We see that C_{zz} is the largest term compared to all the other $C_{\mu\nu}$.

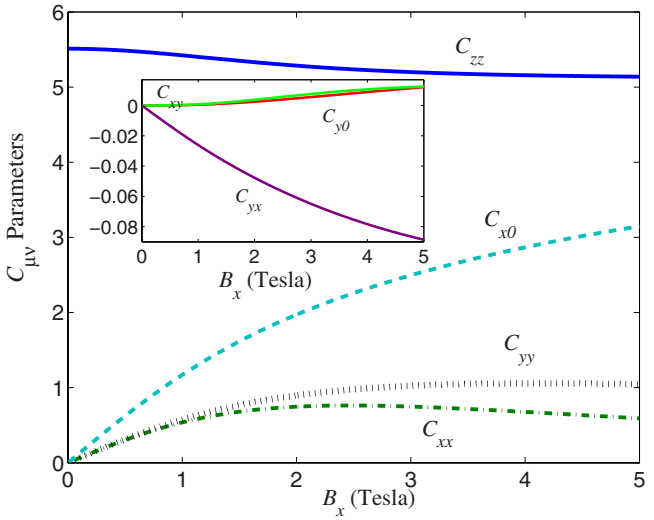

FIG. 4. (Color online) The evolution of the $C_{\mu\nu}$ parameters using the crystal-field V_c from Refs. 16 and 20. In the inset one can see that $C_{xy} \approx C_{y0}$. Coefficients that are not plotted are zero.

For the Hamiltonian in Eq. (5), the J_i^μ operators are substituted by their two-dimensional representations introduced in Eq. (9). This leads to a complicated looking Hamiltonian that acts within the Ising subspace of $|\uparrow\rangle$ and $|\downarrow\rangle$. The projection generates various kinds of interactions among the effective $S_{eff}=\frac{1}{2}$ spins. Via Eq. (7), a specific rotated subspace was chosen, such that $C_{z\mu}=0$ ($\mu=x,y,0$; $\sigma^0 \equiv \mathbb{1}$). As shown in the inset of Fig. 4, C_{xy}, C_{yx}, and C_{y0} are very small, so the interacting terms containing these coefficients can be safely neglected. Neglecting these terms, we obtain

$$\begin{aligned} H_{\text{spin-1/2}} = \frac{1}{2}(g_L\mu_B)^2 \Bigg[& C_{zz}^2(B_x)\sum_{i\neq j} L_{ij}^{zz}\sigma_i^z\sigma_j^z + 2C_{zz}(B_x)C_{xx}(B_x)\sum_{i\neq j} L_{ij}^{zx}\sigma_i^z\sigma_j^x + 2C_{zz}(B_x)C_{yy}(B_x)\sum_{i\neq j} L_{ij}^{zy}\sigma_i^z\sigma_j^y \\ & + C_{xx}^2(B_x)\sum_{i\neq j} L_{ij}^{xx}\sigma_i^x\sigma_j^x + C_{yy}^2(B_x)\sum_{i\neq j} L_{ij}^{yy}\sigma_i^y\sigma_j^y \Bigg] + \frac{1}{2}J_{\text{ex}}\sum_\mu C_{\mu\mu}^2(B_x)\sum_{i,\text{NN}} \sigma_i^\mu\sigma_{\text{NN}}^\mu + (g_L\mu_B)^2 C_{zz}(B_x)C_{x0}(B_x)\sum_{i\neq j} L_{ij}^{zx}\sigma_i^z \\ & + \sum_i \left\{ C_{x0}(B_x)C_{xx}(B_x)\left[4J_{\text{ex}} + (g_L\mu_B)^2\sum_j L_{ij}^{xx}\right] - \frac{\Delta(B_x)}{2}\right\}\sigma_i^x. \end{aligned} \tag{10}$$

When the external magnetic field B_x is equal to zero, only $C_{zz}(0) \neq 0$ and all the other $C_{\mu\nu}$ and $C_{\mu 0}$ are zero (see Fig. 4). Hence, in the absence of an external magnetic field, the system can be described by a simple classical dipolar Ising model.[20] Fortunately, a number of interaction terms are zero or can be neglected with respect to the leading Ising interaction, which is proportional to $C_{zz}^2(B_x)\Sigma_{i\neq j}L_{ij}^{zz}\sigma_i^z\sigma_j^z$. As we can see from Eq. (10), for pure $LiHoF_4$, effective $\sigma_i^x\sigma_j^x$ and $\sigma_i^y\sigma_j^y$ pairwise interactions as well as a linear transverse field along the x direction are induced in the presence of an external magnetic field. As suggested in Fig. 5 and already assumed in Ref. 20, we expect the quantum fluctuations induced by these terms via either dipolar or exchange coupling to be quite small and negligible compared to the quantum fluctuations induced by $\Delta(B_x)$. For the pure (disorder-free) $LiHoF_4$, the invariance of the dipolar interactions under lattice mirror symmetries forces $\Sigma_j L_{ij}^{zx}=0$. So the linear term with $C_{zz}(B_x)C_{x0}(B_x)\Sigma_{i\neq j}L_{ij}^{zx}\sigma_i^z$ vanishes. Considering the

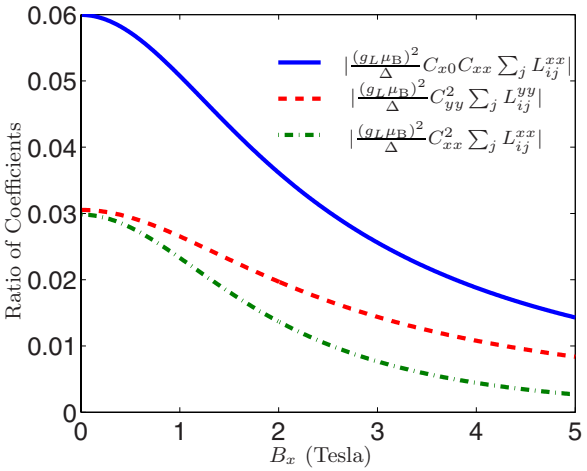

FIG. 5. (Color online) The ratios of the typical values of terms neglected in Hamiltonian (11) with respect to Δ, using the crystal-field V_c from Refs. 16. The dipolar sum is performed using the Ewald method with no demagnetization term.

$C_{zz}(B_x)C_{xx}(B_x)\Sigma_{i\neq j}L_{ij}^{zx}\sigma_i^z\sigma_j^x$ term, again because of lattice mirror symmetry, one has $\Sigma_{i\neq j}L_{ij}^{zx}\sigma_i^z\langle\sigma_j^x\rangle=0$. Therefore this term can contribute only via thermal fluctuations above its vanishing mean-field contribution. Since $\frac{C_{x0}(B_x)}{C_{zz}(B_x)}<1$, we expect the (second-order) fluctuation contribution effects from the above $\sigma_i^z\sigma_j^x$ term to be small. Hence, we neglect the $C_{zz}(B_x)C_{xx}(B_x)\Sigma_{i\neq j}L_{ij}^{zx}\sigma_i^z\sigma_j^x$ term in Eq. (10). We should emphasize that for diluted $LiHo_xY_{1-x}F_4$, since the lattice mirror symmetries are destroyed, the two latter terms, proportional to $\Sigma_{i\neq j}L_{ij}^{zx}\sigma_i^z$ and $\Sigma_{i\neq j}L_{ij}^{zx}\sigma_i^z\langle\sigma_j^x\rangle$, can no longer be neglected.[19,31] Indeed, these are the terms responsible for the generation of the longitudinal random fields[19,30,31] discussed in Sec. I.

Hence, the spin-1/2 Hamiltonian in Eq. (10) can be further simplified to a familiar looking transverse field Ising Hamiltonian with a dipolar and nearest-neighbor exchange Ising interaction,

$$H_{\text{spin-1/2}}=\frac{1}{2}C_{zz}^2(B_x)\left[(g_L\mu_B)^2\sum_{i\neq j}L_{ij}^{zz}\sigma_i^z\sigma_j^z+J_{\text{ex}}\sum_{i,\text{NN}}\sigma_i^z\sigma_{\text{NN}}^z\right]-\frac{\Delta(B_x)}{2}\sum_i\sigma_i^x. \tag{11}$$

To simplify the calculations and in order to be consistent with the notation of Ref. 20 as well as for further comparison between our simulation results and those of Ref. 20, we lump the whole B_x dependence in the transverse-field term. To do so, a renormalization factor $\epsilon(B_x)$ is defined as

$$\epsilon(B_x)=\frac{C_{zz}(B_x)}{C_{zz}(0)}. \tag{12}$$

We renormalize the Hamiltonian as

$$H_{\text{spin-1/2}}=[\epsilon(B_x)]^2\tilde{\mathcal{H}}, \tag{13}$$

with, according to Eq. (11),

$$\tilde{\mathcal{H}}=\frac{1}{2}C_{zz}^2(0)\left[(g_L\mu_B)^2\sum_{i\neq j}L_{ij}^{zz}\sigma_i^z\sigma_j^z+J_{\text{ex}}\sum_{i,\text{NN}}\sigma_i^z\sigma_{\text{NN}}^z\right]-g_L\mu_BC_{zz}(0)\tilde{\mathcal{B}}_x\sum_i\sigma_i^x, \tag{14}$$

where the renormalized effective transverse magnetic field $\tilde{\mathcal{B}}_x$ is related to the real applied B_x via

$$\tilde{\mathcal{B}}_x=\frac{\Delta(B_x)}{2g_L\mu_BC_{zz}(0)[\epsilon(B_x)]^2}, \tag{15}$$

consistent with Ref. 20. In discussing Monte Carlo simulations below, we also define a renormalized temperature $\tilde{T}$ in conjunction with $\tilde{\mathcal{H}}$, with $\tilde{T}$ defined as

$$T=[\epsilon(B_x)]^2\tilde{T}, \tag{16}$$

where T is the real physical temperature.

All results from the Monte Carlo simulations presented in Sec. III B were obtained by considering the renormalized Hamiltonian [Eq. (14)] and performing the simulations with respect to the renormalized $\tilde{T}$ and $\tilde{\mathcal{B}}_x$. Before presenting our Monte Carlo simulations of Eq. (14) pertaining to $LiHoF_4$, we first discuss the technique we employed to handle quantum fluctuations perturbatively for small $\tilde{\mathcal{B}}_x/\tilde{T}$.

B. Effective classical temperature-dependent Hamiltonian: Perturbation expansion

In this section, we focus on the simplified spin-1/2 Hamiltonian in Eq. (14), and aim to implement a cumulant perturbative cumulant Monte Carlo method for this spin-1/2 transverse Ising model.[61,62] For small quantum fluctuations, close to the classical critical temperature, we are able to derive an effective classical Hamiltonian analytically, where quantum fluctuations are incorporated perturbatively. Using such effective perturbative Hamiltonian, we can then perform classical MC simulations. To set the stage, we first consider a general transverse-field Ising Hamiltonian such as

$$\mathcal{H}=\frac{1}{2}\sum_{i,j}\mathcal{L}_{ij}^{zz}\sigma_i^z\sigma_j^z+\frac{1}{2}\mathcal{J}_{\text{ex}}\sum_{i,\text{NN}}\sigma_i^z\sigma_{\text{NN}}^z-\Gamma\sum_i\sigma_i^x-h_0\sum_i\sigma_i^z. \tag{17}$$

Γ is the transverse field in the x direction and h_0 denotes an external longitudinal field along the z direction. For compactness, note that we passed from dipolar interactions denoted $C_{zz}^2(0)(g_L\mu_B)^2L_{ij}^{zz}$ to $\mathcal{L}_{ij}^{zz}$ and from exchange interaction $C_{zz}^2(0)J_{\text{ex}}$ to $\mathcal{J}_{\text{ex}}$ [see Eq. (14)]. The partition function Z for a system with Hamiltonian (17) is

$$Z=\text{Tr}(e^{-\beta\mathcal{H}})=\sum_{\{\psi_i\}}\langle\psi_i|e^{-\beta\mathcal{H}}|\psi_i\rangle, \tag{18}$$

where Z is obtained by tracing over ψ_i which are, for example, direct products of σ^z eigenvectors ($|\uparrow\rangle$ and $|\downarrow\rangle$) and $\beta\equiv1/k_BT$. We can write Hamiltonian (17) as $\mathcal{H}=H_0+H_1$. H_0 is the classical part of the Hamiltonian, for which the ψ_i are eigenvectors. $H_1\equiv-\Gamma\Sigma_i\sigma_i^x$ is the quantum term, which

does not commute with H_0. The existence of these two noncommuting terms in $\mathcal{H}$ prevents us from applying classical Monte Carlo techniques directly to the system. However, we can derive an effective classical Hamiltonian $H_{\text{eff}}[\psi_i]$ as a functional of ψ_i, such that

$$e^{-\beta H_{\text{eff}}[\psi_i]} = \langle \psi_i | e^{-\beta \mathcal{H}} | \psi_i \rangle. \tag{19}$$

Referring to the definition above in Eq. (19), since the right-hand side of Eq. (19) is the matrix element with respect to $|\psi_i\rangle$, $H_{\text{eff}}[\psi_i]$ is a functional depending only on the set of σ_i^z eigenvalues. The partition function can then be written as a classical partition function,

$$Z = \sum_{\{\psi_i\}} e^{-\beta H_{\text{eff}}[\psi_i]}. \tag{20}$$

By finding an explicit expression for $H_{\text{eff}}[\psi_i]$, one can calculate the thermodynamical properties of the system described by $\mathcal{H}$ by performing *classical* Monte Carlo simulations using H_{eff} instead of $\mathcal{H}$.

To proceed, we write the matrix element $\langle \psi | e^{-\beta \mathcal{H}} | \psi \rangle$ in terms of a cumulant expansion,[63]

$$\langle \psi | e^{-\beta \mathcal{H}} | \psi \rangle = \exp\left[-\beta \langle \psi | \mathcal{H} | \psi \rangle + \sum_{n>1}^{\infty} \frac{(-\beta)^n}{n!} \langle \psi | (\mathcal{H} - \langle \psi | \mathcal{H} | \psi \rangle)^n | \psi \rangle \right], \tag{21}$$

where we used $|\psi\rangle$ to mean a typical $|\psi_i\rangle$ eigenvector in order to make the notation more compact. Using Eq. (21), we can derive the effective Hamiltonian $H_{\text{eff}}[\psi_i]$ perturbatively. The details of the derivation of $H_{\text{eff}}[\psi_i]$ are presented in Appendix B. $H_{\text{eff}}[\psi_i]$ is, to order $O(\Gamma^2)$, given by

$$H_{\text{eff}} = H_0 + \beta \Gamma^2 \sum_i \{ \sigma_i^z F_1[2\beta(h_i + h_0)] - F_0[2\beta(h_i + h_0)] \}. \tag{22}$$

In Eq. (22), h_i is the total local field affecting the spin at site i caused by all the other spins and which is

$$h_i = -\sum_{j \neq i} \mathcal{L}_{ij}^{zz} \sigma_j^z - \mathcal{J}_{\text{ex}} \sum_{\text{NN}} \sigma_{\text{NN}}^z, \tag{23}$$

and h_0 is the external longitudinal field in the z direction. The functions $F_0(x)$ and $F_1(x)$ are defined as

$$F_0(x) \equiv \frac{\cosh(x) - 1}{x^2},$$

$$F_1(x) \equiv \frac{\sinh(x) - x}{x^2}. \tag{24}$$

In the effective Hamiltonian H_{eff}, the effect of quantum fluctuations is taken into account perturbatively to order $O(\beta \Gamma^2 / [H_0])$, where $[H_0]$ denotes the order of magnitude of H_0, the classical part (first two and fourth terms) of Eq. (17). To obtain the thermodynamical properties of the system for small transverse fields, we can therefore perform a conventional Monte Carlo simulation using the Metropolis algorithm on the classical temperature-dependent H_{eff}. Since we are interested in thermal averages, we can calculate thermodynamical quantities by differentiating the partition function, which is written in terms of $H_{\text{eff}}[\psi_i]$, with respect to h_0, Γ, or β. The effective Hamiltonian has an explicit h_0 and β dependence. For each true thermodynamical quantum-mechanical quantity, we obtain a pseudo-operator counterpart. For example, the pseudo-operators corresponding to $\langle E \rangle$, $\langle M_z \rangle$, $\langle M_x \rangle$, $\langle M_z^2 \rangle$, and $\langle M_z^4 \rangle$ are calculated in Appendix C, where E, M_z, and M_x are the energy and magnetization operators along the z and x directions, respectively. $\langle \cdots \rangle$ stands for the Boltzmann thermal average.

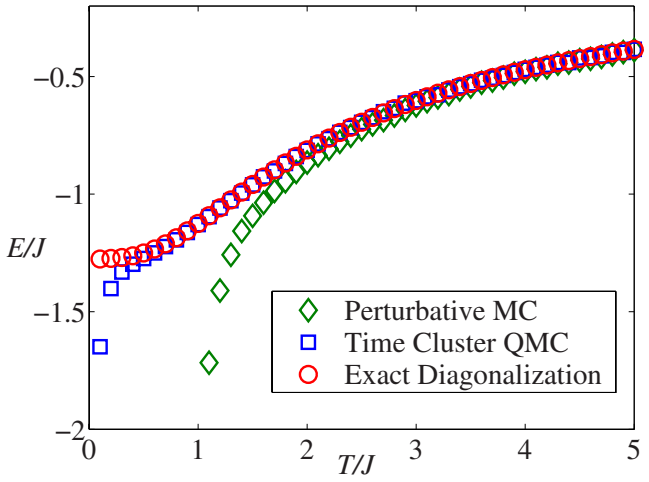

FIG. 6. (Color online) Energy per spin as a function of temperature for a simple one-dimensional nearest-neighbor Ising chain with a transverse field of $\Gamma = J$ and $N = 10$ spins and periodic boundary conditions. The energy is obtained by exact diagonalization of the Hamiltonian, a time-cluster QMC algorithm, and a classical Monte Carlo algorithm of the perturbative effective Hamiltonian.

Because of its perturbative nature in $(\beta\Gamma)$, this method is not reliable for large transverse fields or low temperatures. To illustrate the range of validity of this method, we consider a simple one-dimensional nearest-neighbor transverse-field Ising-model Hamiltonian $H = -J\Sigma_i \sigma_i^z \sigma_{i+1}^z - \Gamma \Sigma_i \sigma_i^x$ with periodic boundary conditions. For a one-dimensional chain of ten ions, we are able to calculate the exact total energy of the chain by exact diagonalization. To check our perturbative MC technique, we calculated the energy of the Ising chain as a function of temperature for a given transverse field. To make a comparison, we also performed a quantum Monte Carlo (QMC) simulation on the system. In this QMC simulation, we used the Trotter-Suzuki[64] formalism and applied a continuous-time-cluster algorithm.[65] In Fig. 6, for a quite large transverse field $\Gamma/J = 1$, we plot the average thermal energy per spin as a function of temperature obtained from exact diagonalization, time-cluster QM, and "perturbative MC" using the effective perturbative Hamiltonian described above. This tests confirms the quantitative correctness of the perturbative Monte Carlo scheme at small $\beta\Gamma^2/J$. Other thermodynamic quantities (e.g., $\langle M_z \rangle$ and $\langle M_x \rangle$) also compare well with the time-cluster QMC and exact diagonalization results.

Before we present our Monte Carlo results for $LiHoF_4$, let us summarize what we have done so far:

(1) Since the spin-spin interactions and $T_c(B_x)$ are small compared to the gap between the low-lying states $|\alpha(B_x)\rangle$ and $|\beta(B_x)\rangle$ with respect to the excited state $|\gamma(B_x)\rangle$, we recast the full microscopic model of $LiHoF_4$ in terms of an effective transverse-field Ising model with effective spin-spin interactions and effective transverse field $\Gamma(B_x)$ that depend on the real physical applied magnetic field B_x.

(2) Since we are interested in a regime where B_x/T_c is small, we develop a perturbation expansion of the partition function in powers of B_x/T. We recast the thermal averages of real physical observables in terms of quantities that can be determined via a classical Monte Carlo simulation of a further effective temperature-dependent classical Hamiltonian.

Having shown that the perturbative cumulant MC can quantitatively describe the TFIM at small $\beta\Gamma^2/[H_0]$, we proceed to Sec. IV to describe how we use this method to study $LiHoF_4$ at small transverse field B_x.

IV. PERTURBATIVE CUMULANT MONTE CARLO STUDY OF $LiHoF_4$

In this section we report results from the perturbative MC simulation to study the low-transverse-field (B_x) properties of $LiHoF_4$ using the low-field perturbative effective Hamiltonian in Eq. (22) and using Eq. (23) for the definition of the local h_i fields. As discussed in Sec. I, our primary goal here is to confirm the quantum Monte Carlo results from the stochastic series expansion in Ref. 20 and the contrasting results with the transverse field B_x phase diagram in Ref. 13 for small B_x (see Fig. 1). Hence, we are indeed interested in $LiHoF_4$ in the case of asymptotically weak B_x/T_c. The temperature we use in our simulations is the renormalized temperature defined in Eq. (16). Regarding Eq. (14), the transverse field Γ used in the perturbative effective Hamiltonian [Eq. (22)] is $\Gamma=g_L\mu_B C_{zz}(0)\tilde{\mathcal{B}}_x$, where $\tilde{\mathcal{B}}_x$ is defined in Eq. (15). For the local field h_i, defined in Eq. (23), we have $\mathcal{L}_{ij}^{zz}=C_{zz}^2(0)(g_L\mu_B)^2L_{ij}^{zz}$ and $\mathcal{J}_{\rm ex}=C_{zz}^2(0)J_{\rm ex}$.

In Sec. IV A, we discuss the reaction-field (RF) and the Ewald summation (ES) methods to deal with long-range dipolar interactions. Then, in Sec. IV B, we explore how the Monte Carlo results in the classical regime, where $B_x=0$, are affected by the choice of the method we use. Next, in Sec. IV C, we discuss the sensitivity of the $J_{\rm ex}$ estimates to finite-size effects and boundary conditions as well as the effect of using different methods (RF or ES) in estimating $J_{\rm ex}$. Finally, in Sec. IV E, we investigate to what extent the final results depend on the set of crystal-field parameters chosen to describe the Ho^{3+} single-ion properties.

A. Reaction-field method versus Ewald summation method

Griffiths' theorem[47] states that in the absence of an external field, the free energy for a dipolar lattice system has to be independent of the sample shape in the thermodynamical limit. Therefore, as an immediate consequence, in the absence of an external field, the net magnetization $\mathcal{M}_z$ of the sample has to be zero. Otherwise, for $\mathcal{M}_z\neq 0$, a shape-dependent demagnetization field would couple to the dipole moments in the sample, making the free energy shape dependent. Here, the demagnetization field is the field originating from the magnetic moments sitting on the boundary of the sample. In the thermodynamic limit, domains form in order for the system to have $\mathcal{M}_z=0$.

Experiments on $LiHoF_4$ showed that the results are shape independent, confirming Griffiths' theorem and domain-wall formation.[66,67] There is evidence that in $LiHoF_4$ long needle-shaped domains form along the c axis.[66,67] If we assume that there is a uniform macroscopic bulk magnetization $\mathcal{M}_z$ within a long needle-shaped domain and the external magnetic field acting on the domain is $B_z^{\rm ext}$, then the susceptibility χ of the domain is

$$\chi=\mathcal{M}_z/B_z^{\rm ext}. \tag{25}$$

It should be noted that the macroscopic bulk magnetization $\mathcal{M}_z$ is given by $\mathcal{M}_z=n_0g_L\mu_B\langle J^z\rangle$, where $n_0=4/a^2c$ is the number of dipoles per unit of volume and where a^2c is the volume of the unit cell. Using $J^z=C_{zz}\sigma^z$, the bulk magnetization $\mathcal{M}_z$ is related to the total moment of the effective Ising spins, $M_z=\Sigma_i\sigma_i^z$, in the $S_{\rm eff}=1/2$ picture by

$$\mathcal{M}_z=\frac{4}{N}\frac{g_L\mu_B C_{zz}(B_x)}{a^2c}\langle M_z\rangle, \tag{26}$$

where N is the total number of dipoles. We consider an imaginary *macroscopic* sphere deep inside a needle-shaped domain. The magnetization inside the sphere should be equal to the uniform bulk magnetization of the long needle-shaped domain. Apart from the external magnetic field $B_z^{\rm ext}$, spins enclosed in the sphere experience an additional field, which originates from the spins on the outer boundary of the imaginary sphere embedded in the long needle-shaped domain. The magnetic surface charge density on the surface of a needle-shaped domain with uniform magnetization $\mathcal{M}_z$ produces an internal magnetic field $B_{\rm needle}=4\pi\mathcal{M}_z$. Meanwhile, the magnetic surface charge density on the surface of the uniformly magnetized sphere with magnetization $\mathcal{M}_z$ induces a (demagnetization) magnetic field $\frac{8\pi}{3}\mathcal{M}_z$ inside the sphere that is in the direction opposite to the applied field and to $B_{\rm needle}$. Therefore, the total field $B_z^{\rm sph}$ inside the spherical cavity is[68]

$$B_z^{\rm sph}=B_z^{\rm ext}-\frac{8\pi}{3}\mathcal{M}_z+4\pi\mathcal{M}_z, \tag{27}$$

with $\mathcal{M}_z$ uniform for a bulk sample. Now, instead of studying the whole needle-shaped bulk sample, we can equivalently study an isolated spherical sample with an effective $B_z^{\rm sph}$ field applied to it. If we substitute $B_z^{\rm ext}$ with $\mathcal{M}_z/\chi$ and $B_z^{\rm sph}$ with $\mathcal{M}_z/\chi_{\rm sph}$, where $\chi_{\rm sph}$ is the susceptibility of the spherical domain, we can write χ as a function of $\chi_{\rm sph}$,

$$\chi=\frac{\chi_{\rm sph}}{1-4\pi\chi_{\rm sph}/3}. \tag{28}$$

If $\chi_{\rm sph}$ is obtained via some calculation procedure for a spherical sample, one can use Eq. (28) to determine the macroscopic susceptibility of the bulk sample within which the sphere is embedded. Specifically, simulations are performed

on a finite-size sphere, and the effect of the macroscopic bulk surrounding the sphere is incorporated in a mean-field manner by considering an effective field B_z^{sph} interacting with the spins inside the spherical sample. Using this method, called the reaction-field (RF) method, Chakraborty *et al.*[20] calculated the finite-size sphere susceptibility χ_{sph} by using the stochastic series-expansion quantum Monte Carlo method.[41] They considered an N-spin system enclosed by a sphere, where the susceptibility of the sphere is obtained from the spin-spin correlation. Referring to Eq. (28), the paramagnetic to ferromagnetic transition (criticality) within the macroscopic long needle-shaped domain occurs at the temperature for which $\chi_{\mathrm{sph}}=\frac{3}{4\pi}$ occurs for a spherical sample. It should be noted that this criterion is derived for macroscopic systems in the thermodynamic limit. Therefore, as discussed in Ref. 51, because of the fluctuation of magnetic moments on the boundary of a finite-size surface, quantities such as specific heat and susceptibility obtained via the RF method are quite sensitive to finite-size effects.

The ES method[49–51] is an alternative approach used to obtain reliable quantitative results for describing real dipolar materials in a periodic boundary condition (PBC).[52,53] In the ES method, the system is modeled by replicating a simulation cell with a linear size of L into a large array of image copies. The ES method generates an effective dipole-dipole interaction $\Sigma_{\mu,\nu}L_{\mathrm{eff}}^{\mu\nu}(\mathbf{r}_{ij})\mu_i^\mu\mu_j^\nu$ between the two magnetic moments $\boldsymbol{\mu}_i$ and $\boldsymbol{\mu}_j$ within the simulation cell. Here, $\boldsymbol{\mu}_i=g_L\mu_B\mathbf{J}_i$ and $\mu,\nu=x,y,z$. This is achieved by periodically replicating the simulation cell with a volume of $\Omega_0=L^3a^2c$ and summing convergently the interactions between the real spins i and j in the specified volume of the simulation cell of dimensionless linear size L and all the periodically repeated images of j as

$$L_{\mathrm{eff}}^{\mu\nu}(\mathbf{r}_{ij})=\sum_{\mathbf{n}}L^{\mu\nu}(\mathbf{r}_{ij}+\mathbf{n}), \tag{29}$$

where $\mathbf{n}=(n_xLa,n_yLa,n_zLc)$ with n_x, n_y, and n_z integers. $L^{\mu\nu}(\mathbf{r}_{ij})=L_{ij}^{\mu\nu}=[\delta^{\mu\nu}|\mathbf{r}_{ij}|^2-3r_{ij}^\mu r_{ij}^\nu]/|\mathbf{r}_{ij}|^5$ are dipolar couplings, which can be written in a more compact form as $L^{\mu\nu}(\mathbf{r}_{ij})=\nabla_i^\mu\nabla_j^\nu|\mathbf{r}_{ij}|^{-1}$. Therefore

$$L_{\mathrm{eff}}^{\mu\nu}(\mathbf{r}_{ij})=\nabla_i^\mu\nabla_j^\nu\sum_{\mathbf{n}}|\mathbf{r}_{ij}+\mathbf{n}|^{-1}. \tag{30}$$

The sum $\Sigma_{\mathbf{n}}|\mathbf{r}_{ij}+\mathbf{n}|^{-1}$ is calculated using the Ewald method, such that the sum contains a real-space sum plus a reciprocal-space sum minus a self-term,[49–51]

$$\sum_{\mathbf{n}}|\mathbf{r}_{ij}+\mathbf{n}|^{-1}=\sum_{\mathbf{n}}\frac{\mathrm{erfc}(\kappa|\mathbf{r}_{ij}+\mathbf{n}|)}{|\mathbf{r}_{ij}+\mathbf{n}|}+\frac{1}{\pi\Omega_0}\sum_{\mathbf{k}\neq0}\frac{4\pi^2}{k^2}e^{-k^2/4\kappa^2}\cos(\mathbf{k}\cdot\mathbf{r}_{ij})-\frac{\kappa}{\sqrt{\pi}}\delta_{ij}. \tag{31}$$

Here $\mathrm{erfc}(x)=(2/\sqrt{\pi})\int_x^\infty e^{-t^2}dt$ and $\mathbf{k}$ denotes the reciprocal vectors of the simulation cell. The convergence factor κ is chosen such that the real-space sum and the reciprocal-space sum converge about equally rapidly.[49–51] The simulation cell and all its replicated images are embedded altogether in a continuous medium. Additionally, each spin experiences a demagnetization field, which originates from the magnetic moments on the boundary of the system.[51] This boundary contribution depends on the shape of the boundary of the macroscopic sample that we are interested in modeling. I.e., for a long needle-shaped sample, the demagnetization field correction to the ES representation of the dipole-dipole interactions is zero.[51] However, for a bulk spherical sample, the magnetic polarization of the magnetic moments on the boundary of the sphere induces a demagnetization field proportional to the magnetization of the sample, $\mathcal{M}_z=\frac{1}{\Omega_0}\Sigma_i\mu_i$, which creates an additional effective field acting on the magnetic moments. The net effect results in an extra effective interaction

$$\frac{4\pi}{2\mu'+1}\frac{\boldsymbol{\mu}_i\cdot\boldsymbol{\mu}_j}{\Omega_0} \tag{32}$$

between magnetic moments $\boldsymbol{\mu}_i$ and $\boldsymbol{\mu}_j$ to be incorporated in the simulation.[51] In practice, the term in Eq. (32) is merely added to the total effective dipolar interaction between spins i and j derived by the ES method. Here, μ' is the magnetic permeability of the surrounding continuum. For a sample surrounded by vacuum, $\mu'=1$.[69 53]

As a result, within the ES method, each spin interacts with all the "real" spins in the specified volume and with all their replicated periodic images. Therefore, one would expect the model treated by the ES method to behave more like a macroscopic system than when using the RF method. However, there are still some finite-size effects due to the artifact of having a periodic sequence of image arrays of finite size L. Once an effective dipole-dipole interaction between spins i and j within the simulation cell has been derived via the ES technique, one can perform Monte Carlo simulations using the standard Metropolis algorithm. Xu *et al.*[70] used this ES technique to simulate long-range dipolar Ising interactions for both the body-centered-cubic (bcc) and body-centered-tetragonal lattices in zero applied field. In a more recent work,[37,38] the ES technique was implemented in a Monte Carlo simulation study of $LiHo_xY_{1-x}F_4$ in zero applied field. In Sec. IV B we discuss the results of MC simulations using the cumulant perturbative method. In our simulations, we incorporate the long-range dipolar interactions using both the RF method as discussed in Ref. 20 and the ES method. The influence of each method on the MC results is investigated in some detail.

B. Cumulant Monte Carlo simulation results

1. Results from reaction-field method

In this subsection we describe the Monte Carlo results obtained using the effective perturbative Hamiltonian [Eq. (22)] by using the reaction-field method for a spherical sample embedded in a long needle-shaped domain and the ES method for a long needle-shaped sample as well as a spherical sample embedded in a long needle-shaped domain. To establish a comparison of the effective perturbative Hamiltonian with previous QMC results,[20] we first performed Monte Carlo simulations for a finite-size sample with

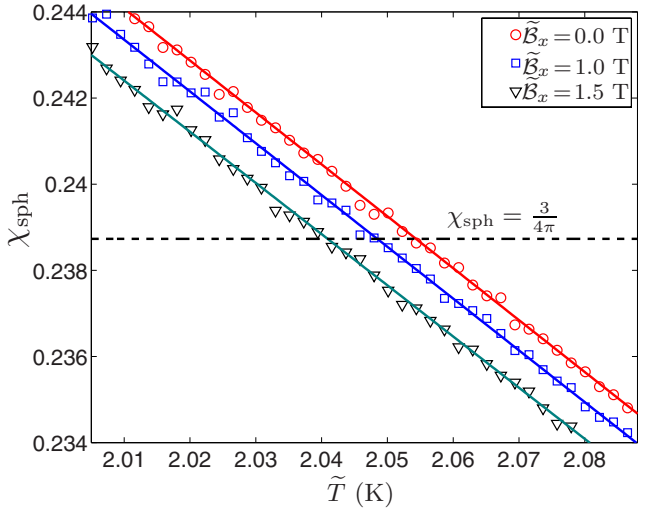

FIG. 7. (Color online) Finding $\widetilde{T}_c$ using the perturbative Monte Carlo method for a sphere of $N=295$ spins and $J_{\rm ex}=0$ and by using the reaction-field $\chi_{\rm sph}=\frac{3}{4\pi}$ criterion at criticality

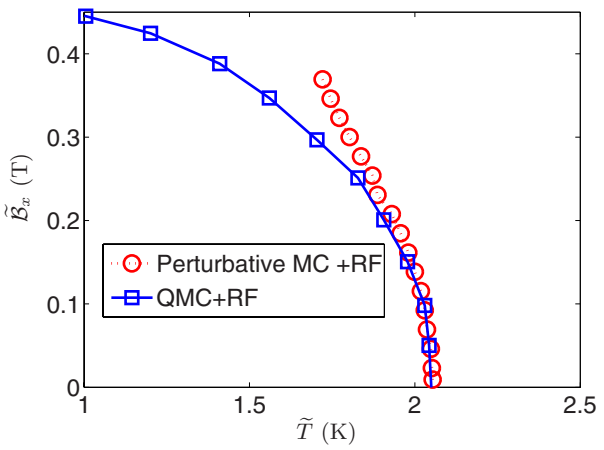

FIG. 8. (Color online) Comparing the phase diagram of the perturbative Monte Carlo method with quantum Monte Carlo results (Ref. 20) as a function of effective temperature and effective magnetic field for a sphere of $N=295$ spins and $J_{\rm ex}=0$, using the reaction-field method of Ref. 20.

open boundary conditions, containing $N=295$ spins, with $J_{\rm ex}$ set to zero. These conditions are identical to the ones of Ref. 20. As shown in Fig. 7 and as similarly done in Ref. 20, we used the reaction-field criterion set by the divergence of χ [see Eq. (28)], $\chi_{\rm sph}=\frac{3}{4\pi}$, to find the effective critical temperature $\widetilde{T}_c(\widetilde{B}_x)$ as a function of the effective field $\widetilde{B}_x$, where $\widetilde{T}$ and $\widetilde{B}_x$ are defined in Eqs. (15) and (16). $\chi_{\rm sph}$ is calculated using

$$\chi_{\rm sph} = \frac{1}{k_B \widetilde{T}} \frac{\alpha}{N} \langle M_z^2 \rangle. \tag{33}$$

The prefactor α is given by

$$\alpha = \frac{4}{a^2 c} [g_L \mu_B C_{zz}(0)]^2. \tag{34}$$

In the perturbative MC method, for determining $\langle M_z^2 \rangle$, we used the pseudo-operator defined by Eq. (C4).

The phase diagram as a function of the effective temperature $\widetilde{T}$ and the effective field $\widetilde{B}_x$, using the effective perturbative Hamiltonian [Eq. (22)] and the above cumulant expansion, is shown in Fig. 8. It can be seen that at low enough fields close to the classical phase transition, our perturbative Monte Carlo results, using the same reaction-field method of Ref. 20, closely match those from the quantum Monte Carlo results of Ref. 20. Using the reaction-field method for $B_x=0$, we get $\widetilde{T}_c=2.03$ K, where $T_c(B_x=0)=\widetilde{T}_c(B_x=0)$ since $\epsilon(B_x=0)=1$.

2. Results from Ewald summation method: Needle-shaped sample

The simulations using the ES method were performed with simulation boxes of size $L=7,8,9$, with each box containing $N=4\times L^3$ spins. The dipolar interactions of ions inside the simulation boxes were derived via the ES technique by assuming an infinitely long needle-shaped sample.[71] That is, the additional demagnetization term correction from Eq. (32) was not incorporated into the Ewald representation of the dipolar interactions between ions i and j. We determined the critical temperature by finding the temperature where the magnetization Binder ratio,[72] $Q=1-\frac{1}{3}\langle M_z^4\rangle/\langle M_z^2\rangle^2$, for system sizes $L=7$, 8, and 9 intersect. The quantities $\langle M_z^4\rangle$ and $\langle M_z^2\rangle$ are calculated using Eqs. (C4) and (C9) within the perturbative effective Hamiltonian scheme. The intersection point in Fig. 9(a) is at the critical temperature $T_c=1.92$ K. As demonstrated in the inset of Fig. 9(a), plotting Q as a function of $L^{1/\nu}(T-T_c)$ shows a good data collapse for system sizes $L=7$, 8, and 9, with the mean-field exponent $\nu=1/2$. This is consistent with the argument that the upper critical dimension for dipolar interactions is $d=3$. A more rigorous analysis of three-dimensional dipolar systems shows logarithmic finite-size scaling corrections.[70,73] We have not investigated these corrections in this study as these are outside the scope of this work. As long as $T_c(B_x\neq 0)>0$, the critical behavior should be controlled by the same critical exponents as for $B_x=0$.[1]

3. Results from combined reaction-field and Ewald summation methods: Spherical sample

We have repeated the perturbative MC simulations using the ES technique but with a slightly different approach. Instead of simulating a long needle-shaped bulk and using the Binder method to obtain the critical temperature, we simulated a sample with a spherical shape. To do so, we derived the effective dipolar interactions between the spins using the ES technique for a sample with spherical boundary. The effect of the spherical boundary is taken into account by incorporating the additional effective interaction in Eq. (32) (Ref. 69) between spins i and j. One can then assume that this spherical sample is embedded in a long needle-shaped bulk. Recalling the derivation of Eq. (28) from Eq. (27), where an effective field $B_z^{\rm sph}$ is applied to the magnetic moments of the sphere, one can determine the macroscopic χ of the bulk by

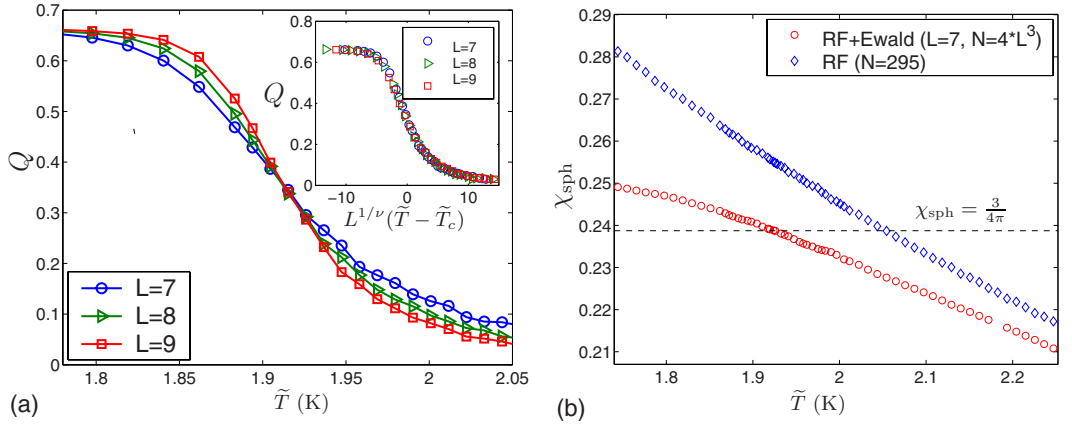

FIG. 9. (Color online) (a) The Binder ratio crossings for $L=7,8,9$ system sizes, obtained by performing MC and using ES technique for a long needle-shaped sample, with $B_x=0$, $J_{ex}=0$. $\widetilde{T}=T$ for $B_x=0$. The inset shows that the Binder ratios collapse for the mean-field exponent $\nu=1/2$ to a very good degree. (b) $\chi_{\rm sph}$ calculated by performing MC simulation, using Eq. (33). The diamonds are results for a finite-size sphere using the reaction-field scheme similar to that in Ref. 20 (i.e., same results as shown in Fig. 7 for the $\widetilde{\mathcal{B}}_x=0$ data). For the circles, we have obtained the interaction between the ions by the ES technique for $L=7$ system size and incorporating the spherical boundary effect via the demagnetization term of Eq. (32) and using $B_x=0$ and $J_{ex}=0$, with again $\widetilde{T}=T$ for $B_x=0$. As one can see, the $\widetilde{T}_c\approx 1.92$ K obtained here agrees with the $\widetilde{T}_c$ obtained using the Binder ratio crossing.

obtaining $\chi_{\rm sph}$ via the ES method for a spherical sample. This procedure is somewhat similar to the one above that employed the reaction field for a finite-size system and which led to the phase diagram in Fig. 8. Yet, there is a difference between this ES calculation and the RF method above. The latter uses a spherical sample with open boundary conditions and considers bare dipolar interactions between a finite number of spins within a finite radius sphere. In the former, a simulation box with periodic boundary conditions is considered. The effective dipolar interactions of ions inside the simulation box are derived via the Ewald summation technique. In this approach a spherical boundary is considered for the whole simulation box and all the replicated images of the real box. In this case, each effective pairwise dipolar interaction described by the ES representation has added to it the extra interaction term given by Eq. (32). Once again, the origin of this additional interaction is the demagnetization field, due to the polarization of the magnetic moments on the spherical boundary. In this approach, the system behaves much more like a macroscopic sphere compared to the reaction-field method used above in Sec. IV B 1 and in Ref. 20. It is further assumed that this macroscopic sphere is embedded inside a long macroscopic needle-shaped domain. By employing the perturbative Monte Carlo method and using Eq. (33), we calculate $\chi_{\rm sph}$ to obtain the critical temperature. Based on Eq. (28), the critical temperature is determined by finding where the $\chi_{\rm sph}=\frac{3}{4\pi}$ criticality criterion is satisfied. As shown in Fig. 9(b), for a simulation box of $L=7$, we obtain $T_c=1.92$ K for a zero transverse field and $J_{ex}=0$, very close to the T_c previously derived using ES technique for a long needle-shaped sample and shown in Fig. 9(a). Thus, the two approaches using ES technique lead to similar results. We believe that the reason for the difference between the classical T_c obtained via ES technique and the $T_c(B_x=0)$ obtained using the reaction-field method[20] is that in the reaction-field method, the number of spins inside the cut-off sphere, which is embedded in the needle-shaped domain, is of too limited size. By using Eq. (28) within the reaction-field method, the effect of the spins on the spherical boundary for a limited size is in essence incorporated in a mean-field manner in the simulation. For a hard, cut-off boundary, thermal fluctuations on the boundary are underestimated, hence resulting in an overestimated T_c. This overestimation of T_c, which decreases with increasing size of the spherical boundary, is expected to vanish in the thermodynamic limit $L\to\infty$.

C. Nearest-neighbor exchange interactions

The zero-transverse-field critical temperature of 1.92 K obtained above lies quite far above the experimental critical temperature of 1.53 K. As suggested by Chakraborty *et al.*,[20] it is reasonable to assume that the discrepancy may be related to a nearest-neighbor antiferromagnetic exchange interaction. Indeed, in the related $LiTbF_4$ material, it has long been known that a nonzero J_{ex} coupling exists in Eqs. (3).[60] There has been no direct determination for the magnitude of this nearest-neighbor exchange in $LiHoF_4$. However, there have been indirect estimations, considering J_{ex} as a free parameter, such that the specific-heat[56] and susceptibility[57] calculations based on mean-field theory fit to the equivalent experimental measurements. Another procedure used to determine J_{ex} would be to fit theoretical calculation with neutron-scattering data, similar to the procedure followed for $LiTbF_4$.[60] Recently, Rønnow *et al.*[16] performed inelastic-neutron-scattering measurements on $LiHoF_4$. Considering J_{ex} as a free parameter, they used the so-called *effective-medium theory* to improve on the parameters estimated from the random-phase approximation. They estimated J_{ex} such that a best fit with the experimental phase diagram is obtained. While for their estimated $J_{ex}=1.16$ mK value there is good agreement with experiment when $2.0<B_x<4.0$ T, as is common in mean-field theory calculations and systematic

improvements such as the effective-medium theory, the critical temperature is overestimated (by 14%) compared with the experimental critical temperature at zero applied field $B_x=0$.

In our work here, we use Monte Carlo techniques and consider the exchange interaction as a free parameter. We can estimate the J_{ex} strength by adjusting its value such that the experimental T_c is reproduced, as was done in Ref. 20. Using the reaction-field method performed for finite spheres in Ref. 20, for $N=295$ spins, $J_{ex}=6.07$ mK was obtained. As a check, we repeated our Monte Carlo simulations, also using the reaction-field method for the same number of spins, and fitted J_{ex} such that the experimental zero-field critical temperature $T_c=1.53$ K is reproduced. We obtained the same $J_{ex}=6.07$ mK as in Ref. 20. It should be noted that, as reported in Ref. 20, one does not obtain a unique J_{ex} value when performing simulations for different sphere sizes. The J_{ex} value strongly depends on the number of spins considered. In Ref. 20, for the largest system size considered ($N=3491$), $J_{ex}=5.25$ mK was required to obtain a Monte Carlo estimate of T_c of 1.53 K. There are two sources of errors that affect the value of the estimated J_{ex} obtained by the reaction-field method of Ref. 20. First, for a given number of spins, when Monte Carlo simulations are performed to calculate T_c, the reaction-field method estimates a higher value for T_c compared to that by the ES method. The sources of these errors are finite-size effects and the underestimation of thermal fluctuations on the boundary, as we now explain. To push down the value of T_c obtained for $J_{ex}=0$ such that it matches the experimental value for T_c, an antiferromagnetic J_{ex} is required. For $J_{ex}=0$, the reaction-field method generates a higher T_c compared to the ES method. Therefore, in order to push down the T_c obtained from Monte Carlo simulation to match the experimental value for T_c, a larger value for the antiferromagnetic J_{ex} is required using the RF method than one required when using the ES method. Second, another source of error affects the J_{ex} value obtained using the reaction-field method. It originates from the number of surface bonds, which depends on the radius of the chosen cutoff sphere. For ions close to the surface, some of the nearest neighbors fall inside the spherical boundary, while some remain outside. Because of the missing number of exchange interactions on the boundary, the overall exchange estimated is forced to be larger than the actual value. When the ES technique is used in conjunction with periodic boundary conditions, this boundary effect problem no longer exists, making the ES technique a more reliable tool for estimating J_{ex}.[52,53] To estimate J_{ex} using our Monte Carlo simulations, we used the Binder ratio crossing method and employed both the ES technique for a long needle-shaped sample and the ES technique for a macroscopic sphere embedded in a long needle-shaped sample. For the latter case, the interactions described by Eq. (32), originating from the magnetic polarizations of the magnetic moments on the spherical boundary, were considered as well. The two J_{ex} values so determined are the same, which are approximately $J_{ex}=3.91$ mK, as illustrated in Fig. 10. Recent Monte Carlo simulations,[37] which also used the Ewald method, found a J_{ex} value in very good agreement with the value that we determine here, once a set is appropriately rescaled by $C_{zz}(B_x=0)^2=5.51^2$ from Fig. 4.

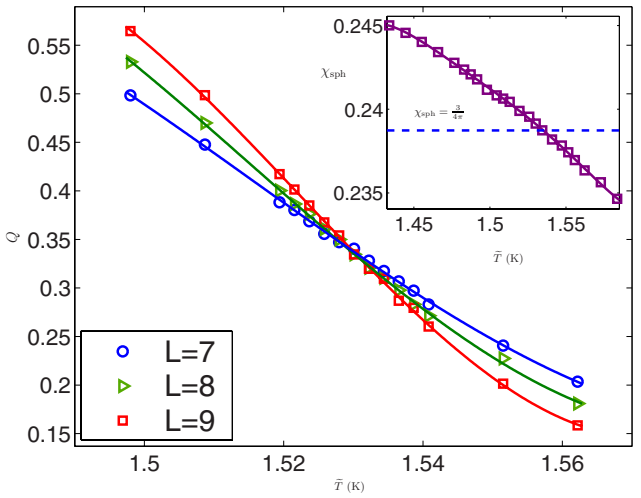

FIG. 10. (Color online) The Binder ratio crossings for $L=7,8,9$ system sizes, obtained by performing MC and using ES technique for a cylindrical boundary with $B_x=0$. $J_{ex}=3.91$ mK is set such that the critical temperature $T_c\approx 1.53$ K is obtained. $\tilde{T}=T$ for $B_x=0$. In the inset χ_{sph} is calculated by performing Monte Carlo simulations, using Eq. (33). The interaction between the ions is obtained by the ES technique for $L=7$ system size and using a spherical boundary condition for $B_x=0$. The same $J_{ex}=3.91$ mK is used and a similar $T_c\approx 1.53$ K is obtained. $\tilde{T}=T$ for $B_x=0$ here.

D. Transverse field versus temperature phase diagram

Having determined a consistent value for J_{ex}, we are now ready to perform Monte Carlo simulations for small transverse magnetic fields B_x. The effect of quantum perturbations is incorporated through the effective Hamiltonian in Eq. (22), which is derived from the renormalized Hamiltonian in Eq. (14). To illustrate the procedure, we show the crossing of the Binder ratio Q for $\tilde{B}_x=0.05$ T and $\tilde{B}_x=0.15$ T in Fig. 11. Equations (15) and (16) are used to obtain the real temperature T and real external transverse magnetic field B_x phase diagram from the effective and $\tilde{B}_x$ values used in the simulations.

Interestingly, using each of the numerical methods discussed above to obtain the phase diagram, it seems that for small B_x the final phase diagrams demonstrating the critical transverse field as a function of temperature are affected very little in respect to the technique used. Figure 12 shows the phase diagrams, using the perturbative Monte Carlo method implementing the reaction-field method and the Ewald summation technique, compared with previous QMC results[20] and experiment.[13] We used Eqs. (15) and (16) to obtain the real physical transverse magnetic field B_x and temperature T from $\tilde{T}$ and $\tilde{B}_x$. As one can see, all the phase diagrams obtained from the effective perturbative method show good agreement with the quantum Monte Carlo result of Chakraborty *et al.*[20] for small transverse fields up to a "real" physical transverse magnetic field $B_x\approx 1.5$ T, at which we presume the lowest-order cumulant formulation of the effective classical Hamiltonian model breaks down. This is the main result of this work.

In conclusion, we: (i) confirm the results of Ref. 20 but, unfortunately, (ii) fail to explain the discrepancy between the

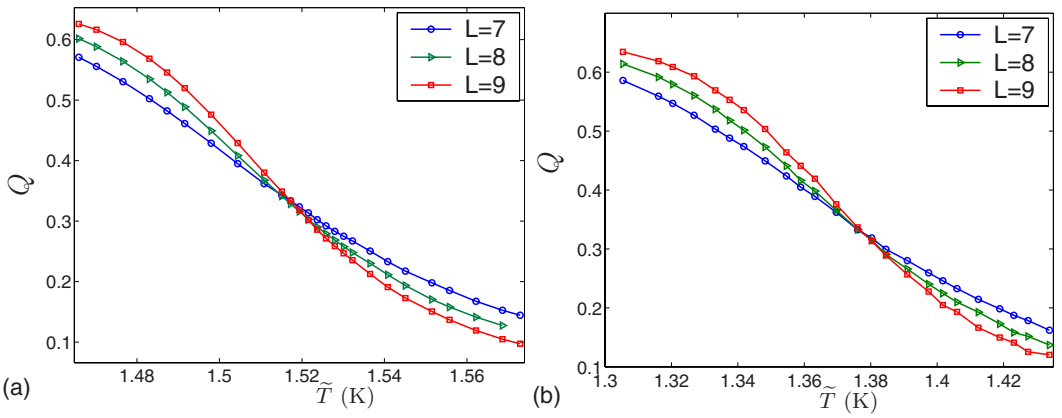

FIG. 11. (Color online) The Binder cumulant crossings for $L=7,8,9$ system sizes, obtained by performing perturbative MC and using ES technique for a long needle-shaped sample with $J_{ex}=3.91$ mK. In (a) we have $\widetilde{B}_x=0.05$ T and in (b) we have $\widetilde{B}_x=0.15$ T.

numerical and experimental results. We are thus led to ponder on theoretical reasons that may explain this discrepancy. We explore one such possibility in Sec. IV E, which is also the one that was put forward in Ref. 20.

E. Other crystal-field parameters

As reported in Ref. 20, we find that the numerical phase diagrams show a discrepancy with the experimental phase diagram, even at asymptotically small transverse fields. Indeed, this was one of the main motivations for the present work. As can be seen in Fig. 12, our efforts in considering (i) a different Monte Carlo scheme and (ii) other ways to handle the long-range dipole-dipole interactions have not allowed us to resolve the discrepancy between the results from numerical simulations of Ref. 20 and the experimental phase diagram of Ref. 13. Chakraborty *et al.*[20] suggested that this discrepancy may be related to uncertainties in the crystal-field parameters. We now briefly explore this possibility.

As discussed in Appendix A, crystal-field parameters are usually obtained such that theoretical calculations match with experimental data from electron-paramagnetic-resonance (EPR),[43] inelastic-neutron-scattering (INS),[16] or susceptibility measurements.[17] Recalling the discussion that led to the derivation of the effective spin-1/2 description of $LiHoF_4$ in Eq. (11), one realizes that the parameters $C_{zz}(B_x)$ and $\Delta(B_x)$ are implicit functions of the crystal-field-level energies and crystal-field-level wave functions. As a result, the mapping of the problem to a spin-1/2 model depends on the chosen values of the B_n^α crystal-field parameters (see Appendix A) entering in the description of the crystal-field Hamiltonian V_c. This state of affairs is made particularly important since, unfortunately, there appears to be some ambiguity in the literature about the empirical values of the B_n^α parameters. All the numerical results that were obtained in Secs. IV B and IV D were based on the set of recent crystal-field parameters reported in Refs. 16 and 20. In another work, EPR spectroscopy experiments were performed on holmium-doped $LiYF_4$ and where the crystal-field parameters were determined.[43] Based on the EPR data reported in Ref. 43, spectral parameters were refined in order to fit the observed dependencies of the resonance frequencies on the external magnetic field, giving a new set of crystal-field parameters and an effective Landé g factor g_L reduced from its pure $^5I_8$ $g_L=5/4$ value down to an effective $g_L^{\text{eff}}=1.21$. Using the alternative set of crystal-field parameters of Ref. 43, as shown in Fig. 13, we obtain alternative values for $C_{zz}(B_x)$ and $\Delta(B_x)$. For example, for $B_x=0$, $C_{zz}(B_x=0)=5.49$ and $\Delta(B_x)=9.85$ K, in comparison with $C_{zz}(B_x=0)=5.51$ and $\Delta(B_x)=10.85$ K, obtained by using the crystal-field parameters (CFPs) of Refs. 16 and 20.

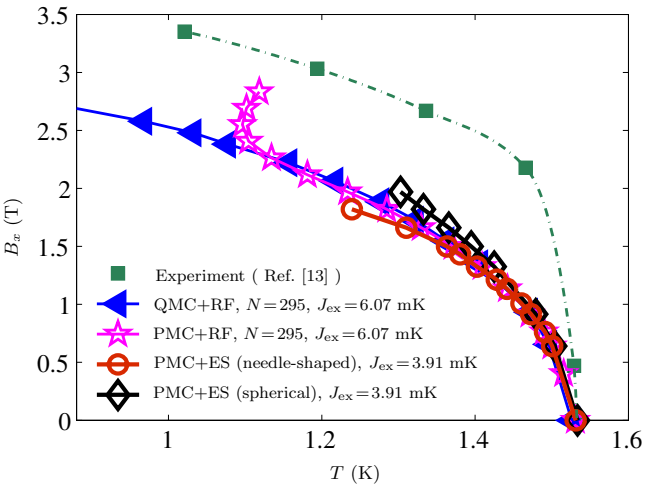

FIG. 12. (Color online) The phase diagrams of the critical transverse field as a function of temperature for $LiHoF_4$. The filled boxes form the experimental phase diagram (Ref. 13). The filled triangles form the phase diagram obtained by QMC (Ref. 20) using the RF method for a finite sphere with $N=295$ spins. The open stars are the results from perturbative Monte Carlo (PMC) method using the same RF method used in Ref. 20 for a sphere with $N=295$ spins. Quite importantly, as discussed in the text, the reaction-field method leads to a considerable overestimate of J_{ex}. The open circles are obtained using the perturbative Monte Carlo method in a needle-shaped domain and using the ES method. The open diamonds are obtained using perturbative Monte Carlo method in a bulk sphere embedded in a needle-shaped domain and using the ES method and the spherical boundary effect in Eq. (32).

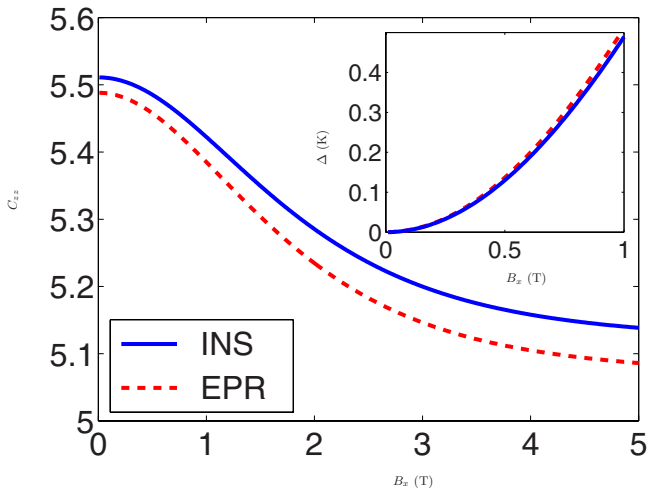

FIG. 13. (Color online) Comparing C_{zz} and Δ as a function of B_x, calculated using two different CFPs. The solid line is obtained, using CFPs from Refs. 16 and 20, based on inelastic-neutron-scattering (INS) experiments. The dashed lines are obtained using the CFPs from Ref. 43, based on EPR experiments.

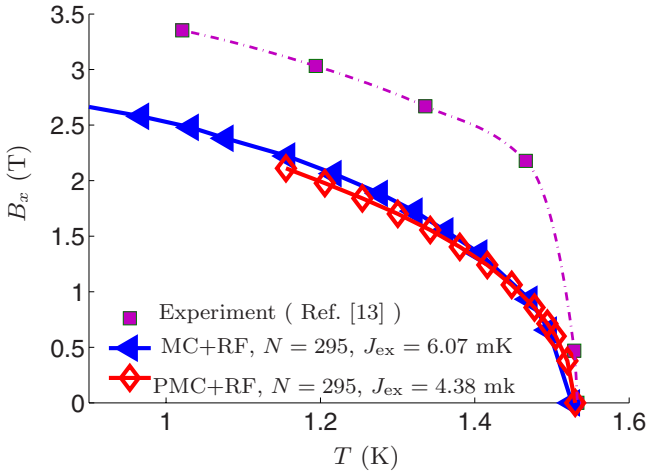

FIG. 14. (Color online) Comparing the phase diagrams of the critical transverse field as a function of temperature for $LiHoF_4$, based on two different sets of crystal-field parameters. The closed triangles are the QMC results of Ref. 20, using the RF method for a finite sphere with $N=295$, based on the CFPs of Ref. 16. The open diamonds are obtained from our perturbative Monte Carlo method, using the same RF method used in Ref. 20 for a sphere with $N=295$ spins, based on the CFPs and g_L^{eff} reported in Ref. 43.

Referring to Eq. (11), one of the consequences of obtaining a different C_{zz} with the new CFPs and using the reduced $g_L^{\text{eff}}=1.21$ is that a different $T_c(B_x=0)$ is obtained. Having determined a different T_c via this new set of CFPs, the value of J_{ex} required to match the experimental $T_c=1.53$ K is different from the $J_{\text{ex}}=3.19$ mK obtained using the CFPs of Ref. 16. It should also be noted that the renormalization factor $\epsilon(B_x)$, which is defined in Eq. (12), is related to $C_{zz}(B_x)$. The value of effective transverse field $\tilde{\mathcal{B}}_x$ defined in Eq. (15) also depends on the values of $C_{zz}(B_x)$, $\Delta(B_x)$, and g_L^{eff}. Therefore, when using the "new" CFPs from Ref. 43, the functions $\epsilon(B_x)$ and $\tilde{\mathcal{B}}_x$ need to be recalculated as well.

We wish to scrutinize "only" the effect of using this new set of CFPs and g_L^{eff} and to compare the resulting phase diagram with the one in Fig. 12 in a rather simple way. To do so, we repeated the perturbative Monte Carlo simulations, using the same reaction-field method used above and in Ref. 20 for a finite-size sphere of $N=295$ spins and a newly determined $J_{\text{ex}}=4.38$ mK. From this new set of CFPs (from Ref. 43), g_L and J_{ex}, a *new* $T_c(B_x)$ phase diagram is derived. This phase diagram is plotted in Fig. 14. As it can be seen, this new phase diagram is consistent with the previous theoretical work (e.g., Ref. 20 and Fig. 12). Interestingly it therefore does not appear at this time that the different crystal-field Hamiltonians available for $LiHoF_4$ (Refs. 16, 17, 20, and 43) are able to explain the significant discrepancy between the B_x-T phase diagram obtained by simulations compared to experimental results of Ref. 13. The key point is that there is essentially no difference between $T_c(B_x)$ phase diagrams using the CFPs and g_L of Ref. 43 provided J_{ex} is adjusted as well. Conversely, different CFPs and g_L^{eff} lead to systematically different $T_c(B_x)$ if J_{ex} is not adjusted.

V. CONCLUSION

We used a perturbative Hamiltonian based on a low-energy effective spin-1/2 description to reinvestigate the B_x-T phase diagram of $LiHoF_4$ for small B_x/T_c where quantum fluctuations are weak. The method we use incorporates perturbatively weak quantum fluctuations within a semiclassical Hamiltonian. Because of its simple tractable form, the method allowed us to address possible factors behind the discrepancy between results from experiments and from previous quantum Monte Carlo simulations in the vicinity of T_c. This method can be easily generalized to more complicated quantum magnetic Ising models, where the Ising-type term is the dominant term and the other noncommuting terms are considered as weak perturbations. For example, the present perturbative method could be directly applicable in studying the effect of nonzero B_x in the diluted $LiHo_xY_{1-x}F_4$ system.

To perform semiclassical Monte Carlo simulations that handle the magnetostatic long-range dipole-dipole interactions properly, we applied the Ewald summation technique for two different system geometries. In order to determine T_c, we used the Binder magnetization ratio crossing for a long needle-shaped sample, and we used the $\chi_{\text{sph}}=\frac{3}{4\pi}$ criterion for a spherical sample embedded inside a long needle-shaped domain. We obtained the same T_c for both cases and, consequently, determined the same value for J_{ex}. The values of the T_c and J_{ex} that we calculated are somewhat different from the T_c and J_{ex} values found in Ref. 20. However, the value of J_{ex} that we determined agrees well with that determined in other recent Monte Carlo simulations that also employ the Ewald method.[37] This difference originates from using open boundary conditions and a finite spherical cutoff in Ref. 20, which underestimates the thermal fluctuations on the boundary. We found that although we used a different method and found a different J_{ex}, the final B_x-T phase diagram obtained here is the same in the low B_x/T_c limit as in the previous results.[20] As a result, we tentatively conclude that the discrepancy between the theoretical and experimental results is *not* of computational origin. To explore a pos-

sible explanation for the discrepancy, we considered a different set of crystal-field parameters.

A consideration of different CFPs, which leads to a different estimate of J_{ex}, does not, however, at the end produce a dramatically different T_c vs B_x phase diagram. This preliminary result, with only a single set of alternative CFPs, goes against the suggestion of Ref. 20 that a possible origin of the discrepancy might be due to the ambiguity in CFPs. It is perhaps surprising that the consideration of a rather different set of CFPs compared to those used in Ref. 20 affects the phase diagram so little once J_{ex} has been readjusted to match the experimental $T_c(B_x=0)=1.53$ K value. Therefore, the origin of the discrepancy between numerics and experiment remains unexplained.

The cumulant Monte Carlo method developed in the present work could be used to carry on further investigation of the cause of the discrepancy. Without this tool, it would have been somewhat less straightforward investigating the relevance of the factors we considered in this paper. The disagreement with the experimental phase diagram of Ref. 13 would suggest that it may be worthwhile to revisit the experimental determination of the B_x vs T_c phase diagram. On the other hand, in both the work presented here and that in Ref. 20, a very simple spin Hamiltonian was considered. Specifically, only long-range magnetostatic dipole-dipole and isotropic (Heisenberg) nearest-neighbor exchange interactions were considered. The faster decreasing $T_c(B_x)$, compared to the experimental case, seems to indicate that there are effects at play in the real material that weaken quantum fluctuations for small B_x, and as B_x is increased from zero. It is quite likely that there exist other couplings in the effective theory in addition to those in the simplest transverse-field Ising model (TFIM) of Eq. (17). As illustrated in Fig. 5, the terms that we ignored when passing from Eq. (10) to Eq. (11) seem too small to be able to resolve this issue. It might be necessary to consider the possibility that not completely negligible anisotropic exchange, higher-order multipolar exchange interaction, or magnetoelastic couplings may be at play in $LiHoF_4$, which could influence the $T_c(B_x)$ phase diagram.

Finally, we note that it would be interesting if one could study other magnetic materials similar to the $LiHoF_4$ compound that could provide another realization of a TFIM. Recently, a mean-field theory calculation concluded that $Ho(OH)_3$, which is an insulating hexagonal dipolar Ising ferromagnet, is very well described by a TFIM when a magnetic field B_x is applied perpendicular to the Ising spin direction.[74] This material constitutes a close analog of $LiHoF_4$ and, when diamagnetically diluted with Y^{3+}, may potentially be an analog of $LiHo_xY_{1-x}F_4$. The existence of another experimental candidate for the study of the TFIM with long-range dipolar interaction presents an opportunity to reinvestigate the puzzling properties of pure and diluted $LiHoF_4$ in a new material, perhaps helping to shed some light on the physics of dipolar Ising systems in both zero and nonzero applied transverse fields. The method we have employed in this work is a suitable tool to study these proposed quantum magnetic Ising materials beyond mean-field theory and provides means to make comparison with future experiments performed on these proposed TFIM materials. To conclude, we hope that the work presented here stimulates further theoretical and experimental studies of $LiHoF_4$ in the regime of small transverse field B_x where the classical paramagnetic to ferromagnetic transition is only perturbatively affected by B_x.

ACKNOWLEDGMENTS

We thank P. Chakraborty, J.-Y. Fortin, S. Girvin, P. Henelius, R. Hill, B. Malkin, P. McClarty, J. Quilliam, P. Stasiak, and F. Vernay for useful discussions. Support for this work was provided by the Canada Research Chair Program (Tier I, M.J.P.G.), the Canada Foundation for Innovation, the Ontario Innovation Trust, the Canadian Institute for Advanced Research, and NSERC of Canada.

APPENDIX A

In this appendix, we briefly discuss how the crystal-field Hamiltonian of $LiHoF_4$ can be written in terms of angular momentum operators and crystal-field parameters. In the point-charge approximation description of the crystal field, we assume that the ions interacting with Ho^{3+} electrostatically are point charges. The potential at $\mathbf{r}$ is simply the sum of point-charge Coulomb interaction potential,

$$V(\mathbf{r}) = \sum_i \frac{q_i}{|\mathbf{R}_i - \mathbf{r}|}, \tag{A1}$$

where $\mathbf{R}_i$ is the position and the total electric charge of the ith ion. $V(\mathbf{r})$ can be expanded as

$$V(r,\theta,\phi) = \sum_{n=0}^{\infty} \sum_{\alpha} r^n \gamma_{n\alpha} Z_{n\alpha}(\theta,\phi), \tag{A2}$$

where

$$\gamma_{n\alpha} = \sum_i \frac{4\pi q}{(2n+1)} \frac{Z_{n\alpha}(\theta_i,\phi_i)}{R_i^{n+1}}, \tag{A3}$$

and the $Z_{n\alpha}$ are the spherical harmonics.[75] To get the crystal-field Hamiltonian V_c, one must sum this energy over all of the valence electrons of the holmium (Ho^{3+}) moments. Hence we have

$$V_C = -e \sum_j V(\mathbf{r}_j). \tag{A4}$$

According to arguments provided by Stevens[76] for evaluating the matrix elements of the crystal-field Hamiltonian between wave functions specified by the angular momentum $\mathbf{J}$, the crystal-field Hamiltonian can be written in terms of the Stevens operator equivalents O_n^α, built out of the vector components of $\mathbf{J}$ operators,

$$V_C = \sum_{n,\alpha} B_n^\alpha O_n^\alpha. \tag{A5}$$

The Stevens equivalent operators act on the angular momentum states of the wave functions. The matrix element of the radial part of the wave function is incorporated in the B_n^α parameters, usually determined by fitting to experimental

(e.g., spectroscopic) data.[16,17,43] From angular momentum algebra, in the case of $4f$ electrons, we need to consider only $n=0,2,4,6$ in sum (A5).

The choice of B_n^α coefficients in Hamiltonian (A5) that do not vanish and have nonzero corresponding matrix elements is dictated by the point symmetry group of the crystalline environment. The details of the method and conventions for expressing the crystal-field Hamiltonian can be found in the review paper by Hutchings.[75] The point-group symmetry of $LiHoF_4$ is S_4 symmetry, which means the lattice is invariant respect to a $\frac{\pi}{2}$ rotation about the z axis and reflection with respect to the x-y plane. The crystal-field Hamiltonian for $LiHoF_4$ is therefore written as

$$V_C = B_2^0 O_2^0 + B_4^0 O_4^0 + B_4^{4C} O_4^{4C} + B_4^{4S} O_4^{4S} + B_6^0 O_6^0 + B_6^{4C} O_6^{4C} + B_6^{4S} O_6^{4S}. \tag{A6}$$

The relevant operator equivalents are given in terms of angular momentum operators[75] (J_z, J_+, J_-, and J^2) by

$$O_2^0 = 3J_z^2 - J^2,$$

$$O_4^0 = 35Jz^4 - 30J^2J_z^2 + 25J_z^2 - 6J^2 + 3J^4,$$

$$O_4^{4C} = \frac{1}{2}(J_+^4 + J_-^4),$$

$$O_4^{4S} = \frac{1}{2i}(J_+^4 - J_-^4),$$

$$O_6^0 = 231J_z^6 - 315J^2J_z^4 + 735J_z^4 + 105J^4J_z^2 - 525J^2J_z^2 + 294J_z^2 - 5J^6 + 40J^4 - 60J^2,$$

$$O_6^{4C} = \frac{1}{4}(J_+^4 + J_-^4)(11J_z^2 - J^2 - 38) + \text{H.c.},$$

and

$$O_6^{4S} = \frac{1}{4i}(J_+^4 - J_-^4)(11J_z^2 - J^2 - 38) + \text{H.c.} \tag{A7}$$

The B_n^α parameters are chosen such that the resulting energy levels match those determined from spectroscopic data. Two different sets of experimentally determined crystal-field parameters are given in Table I. The first set of the parameters was determined by inelastic neutron scattering reported in Ref. 16 and implemented in the calculations presented in this work as well as in Ref. 20. The next set of B_n^α parameters were determined from an analysis of electron paramagnetic resonance (EPS) data[43] and used in the calculations of Sec. IV E.

TABLE I. The first column contains the CFPs for $LiHoF_4$ determined experimentally by fitting the results of random-phase approximation spin-wave dynamics calculation to neutron-scattering data from Ref. 16. The second column contains the crystal-field parameters estimated using EPR spectroscopy experiment (Ref. 43).

Parameter	Ref. 16	Ref. 43
B_2^0	−0.696 K	−0.609 K
B_4^0	4.06×10^{-3} K	3.75×10^{-3} K
B_4^{4C}	4.18×10^{-2} K	3.15×10^{-2} K
B_4^{4S}	0 K	2.72×10^{-2} K
B_6^0	4.64×10^{-6} K	6.05×10^{-6} K
B_6^{4C}	8.12×10^{-4} K	6.78×10^{-4} K
B_6^{4S}	1.137×10^{-4} K	4.14×10^{-4} K

APPENDIX B

In this appendix, starting from Eq. (21), we give the details of the derivation of the effective perturbative Hamiltonian $H_{\text{eff}}[\psi_i]$ obtained from a cumulant expansion when quantum fluctuations are small. Deriving $H_{\text{eff}}[\psi_i]$, as defined by Eq. (20), one can rewrite the partition function of the system in a classical form.

Referring to Eq. (21), recalling that $|\psi\rangle$ is a direct product of σ_i^z eigenstates, the expectation value $\langle\psi|\sigma^x|\psi\rangle$ is zero, so $\langle\psi|\mathcal{H}|\psi\rangle = \langle\psi|H_0|\psi\rangle$. Defining $E_0(\psi) \equiv \langle\psi|H_0|\psi\rangle$, we can write $\langle\psi|(\mathcal{H} - \langle\psi|\mathcal{H}|\psi\rangle)^n|\psi\rangle = \langle\psi|[\mathcal{H} - E_0(\psi)]^n|\psi\rangle$.

Performing a polynomial expansion on $[\mathcal{H} - E_0(\psi)]^n = \{[H_0 - E_0(\psi)] + H_1\}^n$ and keeping terms to order $O(\Gamma^2)$ in the polynomial expansion ($H_1 \propto \Gamma$), we have

$$\begin{aligned}\langle\psi|[\mathcal{H} - E_0(\psi)]^n|\psi\rangle &= \langle\psi|\{[H_0 - E_0(\psi)] + H_1\}^n|\psi\rangle \\ &\approx \sum_{n_1,n_2,n_3} \delta(n_1 + n_2 + n_3, n-2) \\ &\quad \times [\langle\psi|[H_0 - E_0(\psi)]^{n_1} H_1 [H_0 \\ &\quad - E_0(\psi)]^{n_2} H_1 [H_0 - E_0(\psi)]^{n_3}|\psi\rangle] \\ &= \langle\psi|H_1[H_0 - E_0(\psi)]^{n-2} H_1|\psi\rangle. \end{aligned} \tag{B1}$$

To write Eq. (B1) we have used the fact that

$$\langle\psi|[H_0 - E_0(\psi)]^n|\psi\rangle = 0 \tag{B2}$$

and

$$\langle\psi|[H_0 - E_0(\psi)]^m H_1 [H_0 - E_0(\psi)]^k|\psi\rangle = 0 \tag{B3}$$

for integer numbers m and k. The effect of σ_i^x on $|\psi\rangle$ is to flip the spin i. We define $\sigma_i^x|\psi\rangle = |f_i\psi\rangle$, where $f_i\psi$ means that the ith spin has flipped, such that if the ith spin was in the $|\uparrow\rangle$ or the $|\downarrow\rangle$ eigenstate of σ_i^z, it changes into the $|\downarrow\rangle$ or $|\uparrow\rangle$ state, respectively. In Eq. (B1), using $H_1 = -\Gamma\Sigma_i\sigma_i^x$, we get

$$\begin{aligned}&\langle\psi|H_1[H_0 - E_0(\psi)]^{n-2} H_1|\psi\rangle \\ &= \Gamma^2 \sum_{i,j} \langle\psi|\sigma_i^x[H_0 - E_0(\psi)]^{n-2}\sigma_j^x|\psi\rangle \\ &= \Gamma^2 \sum_{i,j} \langle f_i\psi|[H_0 - E_0(\psi)]^{n-2}|f_j\psi\rangle. \end{aligned} \tag{B4}$$

Here $\langle f_i\psi|[H_0 - E_0(\psi)]^{n-2}|f_j\psi\rangle$ is zero unless $i=j$. Thus, Eq. (B1) can be written as

$$\langle\psi|[\mathcal{H}-E_0(\psi)]^n|\psi\rangle=\Gamma^2\sum_i[E_0(f_i\psi)-E_0(\psi)]^{n-2}. \quad \text{(B5)}$$

Considering the definition of H_{eff}, by substituting $E_0(f_i\psi)-E_0(\psi)=2(h_i+h_0)\sigma_i^z$ into Eq. (21), we obtain

$$H_{\text{eff}}=H_0-\beta\Gamma^2\sum_i\sum_{n>1}^{\infty}\frac{1}{n!}[-2\beta(h_i+h_0)]^{n-2}$$

$$=H_0+\beta\Gamma^2\sum_i\{\sigma_i^zF_1[2\beta(h_i+h_0)]-F_0[2\beta(h_i+h_0)]\}. \quad \text{(B6)}$$

In Eq. (B6), h_i is the total local field affecting the spin at site i by other spins, which is

$$h_i=-\sum_{j\neq i}\mathcal{L}_{ij}^{zz}\sigma_j^z-\mathcal{J}_{\text{ex}}\sum_{\text{NN}}\sigma_{\text{NN}}^z, \quad \text{(B7)}$$

and h_0 is the external longitudinal field in the z direction. The functions $F_0(x)$ and $F_1(x)$ are defined as

$$F_0(x)=\frac{\cosh(x)-1}{x^2},$$

$$F_1(x)=\frac{\sinh(x)-x}{x^2}. \quad \text{(B8)}$$

APPENDIX C

In this appendix, we establish the relationship between the real thermodynamical quantities as physical observables and their corresponding pseudo-operator representation, which are obtained using the perturbative effective classical Hamiltonian in Eq. (22). These thermodynamical quantities are calculated by employing the derived pseudo-operators in our perturbative classical Monte Carlo simulations.

Writing the partition function in terms of the perturbative effective Hamiltonian $H_{\text{eff}}[\psi_i]$, the pseudo-operators corresponding to $\langle E\rangle$, $\langle M_z\rangle$, $\langle M_x\rangle$, $\langle M_z^2\rangle$, and $\langle M_z^4\rangle$, which should be calculated to obtain thermodynamical quantities using Monte Carlo simulations, are written as

$$\langle E\rangle=-\frac{1}{Z}\frac{\partial Z}{\partial\beta}=\left\langle H_{\text{eff}}+\beta\frac{\partial H_{\text{eff}}}{\partial\beta}\right\rangle, \quad \text{(C1)}$$

$$\langle M_z\rangle=\left\langle-\frac{\partial H_{\text{eff}}}{\partial h_0}\right\rangle, \quad \text{(C2)}$$

$$\langle M_x\rangle=\left\langle-\frac{\partial H_{\text{eff}}}{\partial\Gamma}\right\rangle, \quad \text{(C3)}$$

$$\langle M_z^2\rangle=\left\langle\left(\frac{\partial H_{\text{eff}}}{\partial h_0}\right)^2-\frac{1}{\beta}\frac{\partial^2H_{\text{eff}}}{\partial h_0^2}\right\rangle, \quad \text{(C4)}$$

$$\langle M_z^4\rangle=\frac{1}{\beta^4}\left\langle-\beta\frac{\partial^4H_{\text{eff}}}{\partial h_0^4}+4\beta^2\frac{\partial^3H_{\text{eff}}}{\partial h_0^3}\frac{\partial H_{\text{eff}}}{\partial h_0}\right.$$

$$-6\beta^3\frac{\partial^2H_{\text{eff}}}{\partial h_0^2}\left(\frac{\partial H_{\text{eff}}}{\partial h_0}\right)^2+3\beta^2\left(\frac{\partial^2H_{\text{eff}}}{\partial h_0^2}\right)^2 \quad \text{(C5)}$$

$$\left.+\quad\beta^4\left(\frac{\partial H_{\text{eff}}}{\partial h_0}\right)^4\right\rangle, \quad \text{(C6)}$$

where E, M_z, and M_x are the energy and magnetization in the z and x directions and their equivalent pseudo-operators which should be calculated via the classical Monte Carlo simulation are on right. The thermal average is denoted by $\langle\cdots\rangle$. Applying the derivatives and using the perturbative effective Hamiltonian [Eq. (22)], we find

$$E=E_0+2\beta\Gamma^2\sum_i\{\sigma_i^zF_1[2\beta(h_i+h_0)]-F_0[2\beta(h_i+h_0)]\}$$

$$+\beta\Gamma^2\sum_i2\beta(h_i+h_0)\{\sigma_i^zF_1^{(1)}[2\beta(h_i+h_0)]$$

$$-F_0^{(1)}[2\beta(h_i+h_0)]\}, \quad \text{(C7)}$$

while

$$M_x=-2\beta\Gamma\sum_i\{\sigma_i^zF_1[2\beta(h_i+h_0)]-F_0[2\beta(h_i+h_0)]\} \quad \text{(C8)}$$

and

$$M_z=\sum_i\sigma_i^z-2\beta^2\Gamma^2\sum_i\{\sigma_i^zF_1^{(1)}[2\beta(h_i+h_0)]$$

$$-F_0^{(1)}[2\beta(h_i+h_0)]\}, \quad \text{(C9)}$$

with $F_i^{(n)}(x)$ defined as $F_i^{(n)}=\frac{d^nF_i(x)}{dx^n}$, where $i=1,0$.

In order to find an expression for $\langle M_z^2\rangle$ and $\langle M_z^4\rangle$, we need to calculate $\frac{\partial H_{\text{eff}}}{\partial h_0}$, $\frac{\partial^2H_{\text{eff}}}{\partial h_0^2}$, $\frac{\partial^3H_{\text{eff}}}{\partial h_0^3}$, and $\frac{\partial^4H_{\text{eff}}}{\partial h_0^4}$. We find

$$\frac{\partial H_{\text{eff}}}{\partial h_0}=-\sum_i\sigma_i^z+2\beta^2\Gamma^2\sum_i\{\sigma_i^zF_1^{(1)}[2\beta(h_i+h_0)]$$

$$-F_0^{(1)}[2\beta(h_i+h_0)]\}, \quad \text{(C10)}$$

$$\frac{\partial^2H_{\text{eff}}}{\partial h_0^2}=4\beta^3\Gamma^2\sum_i\{\sigma_i^zF_1^{(2)}[2\beta(h_i+h_0)]-F_0^{(1)}[2\beta(h_i+h_0)]\}, \quad \text{(C11)}$$

$$\frac{\partial^3H_{\text{eff}}}{\partial h_0^3}=8\beta^4\Gamma^2\sum_i\{\sigma_i^zF_1^{(3)}[2\beta(h_i+h_0)]-F_0^{(3)}[2\beta(h_i+h_0)]\}, \quad \text{(C12)}$$

and

$$\frac{\partial^4H_{\text{eff}}}{\partial h_0^4}=16\beta^5\Gamma^2\sum_i\{\sigma_i^zF_1^{(4)}[2\beta(h_i+h_0)]-F_0^{(4)}[2\beta(h_i+h_0)]\}. \quad \text{(C13)}$$

[1] S. Sachdev, *Quantum Phase Transitions* (Cambridge University Press, Cambridge, England, 1999).
[2] S. L. Sondhi, S. M. Girvin, J. P. Carini, and D. Shahar, Rev. Mod. Phys. **69**, 315 (1997).
[3] R. J. Elliott, P. Pfeuty, and C. Wood, Phys. Rev. Lett. **25**, 443 (1970).
[4] B. K. Chakrabarti, A. Dutta, and P. Sen, *Quantum Ising Phases and Transitions in Transverse Ising Models* (Springer-Verlag, Heidelberg, 1996).
[5] P. G. de Gennes, Solid State Commun. **1**, 132 (1963).
[6] K. Binder and A. P. Young, Rev. Mod. Phys. **58**, 801 (1986).
[7] H. G. Ballesteros, A. Cruz, L. A. Fernandez, V. Martin-Mayor, J. Pech, J. J. Ruiz-Lorenzo, A. Tarancon, P. Tellez, C. L. Ullod, and C. Ungil, Phys. Rev. B **62**, 14237 (2000).
[8] H. Rieger and A. P. Young, Phys. Rev. Lett. **72**, 4141 (1994).
[9] H. Rieger and A. P. Young, Phys. Rev. B **54**, 3328 (1996).
[10] M. Guo, R. N. Bhatt, and D. A. Huse, Phys. Rev. B **54**, 3336 (1996).
[11] R. B. Griffiths, Phys. Rev. Lett. **23**, 17 (1969).
[12] B. M. McCoy, Phys. Rev. Lett. **23**, 383 (1969).
[13] D. Bitko, T. F. Rosenbaum, and G. Aeppli, Phys. Rev. Lett. **77**, 940 (1996).
[14] W. Wu, B. Ellman, T. F. Rosenbaum, G. Aeppli, and D. H. Reich, Phys. Rev. Lett. **67**, 2076 (1991).
[15] H. M. Rønnow, R. Parthasarathy, J. Jensen, G. Aeppli, T. F. Rosenbaum, and D. F. McMorrow, Science **308**, 389 (2005).
[16] H. M. Rønnow, J. Jensen, R. Parthasarathy, G. Aeppli, T. F. Rosenbaum, D. F. McMorrow, and C. Kraemer, Phys. Rev. B **75**, 054426 (2007).
[17] P. E. Hansen, T. Johansson, and R. Nevald, Phys. Rev. B **12**, 5315 (1975).
[18] A. Chin and P. R. Eastham, arXiv:cond-mat/0610544 (unpublished).
[19] S. M. A. Tabei, F. Vernay, and M. J. P. Gingras, Phys. Rev. B **77**, 014432 (2008).
[20] P. B. Chakraborty, P. Henelius, H. Kjønsberg, A. W. Sandvik, and S. M. Girvin, Phys. Rev. B **70**, 144411 (2004).
[21] D. M. Silevitch, D. Bitko, J. Brooke, S. Ghosh, G. Aeppli, and T. F. Rosenbaum, Nature (London) **448**, 567 (2007).
[22] D. H. Reich, B. Ellman, J. Yang, T. F. Rosenbaum, G. Aeppli, and D. P. Belanger, Phys. Rev. B **42**, 4631 (1990).
[23] We note that the existence of a spin-glass transition in $LiHo_xY_{1-x}F_4$ ($x=0.167$) in zero transverse magnetic field has very recently been questioned. See Ref. 24.
[24] P. E. Jönsson, R. Mathieu, W. Wernsdorfer, A. Tkachuk, and B. Barbara, Phys. Rev. Lett. **98**, 256403 (2007).
[25] C. Ancona-Torres, D. M. Silevitch, G. Aeppli, and T. F. Rosenbaum, Phys. Rev. Lett. **101**, 057201 (2008).
[26] Recently, another group released a report that $LiHo_xY_{1-x}F_4$ ($x=0.045$) behaves like a rather conventional spin glass system in contrast with the no spin glass transition scenario of Ref. 24 and also in contrast with the antiglass proposal of Refs. 22 and 34. (See J. A. Quilliam, S. Meng, C. G. A. Mugford, and J. B. Kycia, Phys. Rev. Lett. **101**, 187204 (2008).
[27] J. Brooke, Ph.D. thesis, University of Chicago, 2000.
[28] J. A. Mydosh, *Spin Glasses: An Experimental Introduction* (Taylor & Francis, London, 1993).
[29] W. Wu, Ph.D. thesis, University of Chicago, 1992.
[30] M. Schechter and N. Laflorencie, Phys. Rev. Lett. **97**, 137204 (2006).
[31] S. M. A. Tabei, M. J. P. Gingras, Y.-J. Kao, P. Stasiak, and J.-Y. Fortin, Phys. Rev. Lett. **97**, 237203 (2006).
[32] M. Schechter, P. C. E. Stamp, and N. Laflorencie, J. Phys.: Condens. Matter **19**, 145218 (2007).
[33] S. Ghosh, R. Parthasarathy, T. F. Rosenbaum, and G. Aeppli, Science **296**, 2195 (2002).
[34] S. Ghosh, T. F. Rosenbaum, G. Aeppli, and S. N. Coppersmith, Nature (London) **425**, 48 (2003).
[35] M. J. Stephen and A. Aharony, J. Phys. C **14**, 1665 (1981).
[36] J. Snider and C. C. Yu, Phys. Rev. B **72**, 214203 (2005).
[37] A. Biltmo and P. Henelius, Phys. Rev. B **76**, 054423 (2007).
[38] A. Biltmo and P. Henelius, Phys. Rev. B **78**, 054437 (2008).
[39] While Ref. 24 reported a lack of spin-glass transition in $LiHo_xY_{1-x}F_4$ for $x=0.045$ and $x=0.165$, more recent work affirmed that there is indeed a spin-glass transition in that material for $x=0.167$ and 0.198 when $B_x=0$ (see Ref. 25); Yet, an even more recent paper by the authors of Ref. 24 reiterated that there is no thermodynamic spin-glass transition in this material when $x \lesssim 0.2$ [P. E. Jönsson, R. Mathieu, W. Wernsdorfer, A. M. Tkachuk, and B. Barbara, arXiv:0803.1357 (unpublished)]. At this time, the experimental situation therefore appears rather controversial.
[40] A recent large scale Monte Carlo study finds, at variance with Refs. 36–38, evidence for a thermodynamic spin glass transition at nonzero temperature in a model of $LiHo_xY_{1-x}F_4$. See K.-M. Tam and M. J. P. Gingras, arXiv:0810.0854 (unpublished).
[41] A. W. Sandvik and J. Kurkijårvi, Phys. Rev. B **43**, 5950 (1991); A. W. Sandvik, Phys. Rev. E **68**, 056701 (2003).
[42] M. Schechter and P. C. E. Stamp, Phys. Rev. Lett. **95**, 267208 (2005).
[43] G. S. Shakurov, M. V. Vanyunin, B. Z. Malkin, B. Barbara, R. Yu. Abdulsabirov, and S. L. Korableva, Appl. Magn. Reson. **28**, 251 (2005).
[44] L. N. Kantorovich and I. I. Tupitsyn, J. Phys.: Condens. Matter **11**, 6159 (1999).
[45] The sum of an infinite number of dipole-dipole interactions is conditionally convergent and depends on the order of the summation. For example, if the dipole-dipole interactions of a central unit cell with unit cells located on an ever-increasingly long needle-shaped sample are summed up, the energy converges to a value different from that if the interaction energies had been summed spherically. Roughly speaking, this conditional convergence arises because the number of interacting dipoles on a shell of radius R grows like R^2, while the strength of a single dipole-dipole interaction falls like $1/R^3$, and the mathematical $\Sigma_{n=1}^{\infty} \frac{1}{n}$ summation diverges. The value that the sum converges to depends on the shape of the boundary of the system. The effect of the geometry of the boundary is incorporated in the Ewald summation technique. See Ref. 44.
[46] J. M. Luttinger and L. Tisza, Phys. Rev. **70**, 954 (1946).
[47] R. Griffiths, Phys. Rev. **176**, 655 (1968).
[48] J. A. Barker and R. O. Watts, Mol. Phys. **26**, 789 (1973).
[49] J. M. Ziman, *Principles of the Theory of Solids*, 2nd ed. (Cambridge University Press, Cambridge, England, 1972).
[50] M. Born and S. Huang, *Dynamical Theory of Crystal Lattices* (Oxford University Press, New York, 1968).
[51] S. W. de Leeuw, J. W. Perram, and E. R. Smith, Annu. Rev. Phys. Chem. **37**, 245 (1986).
[52] For example, the Ewald summation method has proved quite efficient to allow a characterization of the thermodynamic prop-

erties of rare-earth spin ice materials, such as $Ho_2Ti_2O_7$ and $Dy_2Ti_2O_7$, and a determination of the exchange in these materials. See Ref. 53 and references therein.

[53] R. G. Melko and M. J. P. Gingras, J. Phys.: Condens. Matter **16**, R1277 (2004).

[54] J. Jensen and A. R. Mackintosh, *Rare Earth Magnetism* (Oxford University Press, Oxford, 1991).

[55] The QMC method based on stochastic series expansion (SSE) in Ref. 41 amounts to a numerical summation of βH to high powers, where H is the Hamiltonian and $\beta=1/k_BT$. The method we use splits H into the classical Ising sector H_0 and the quantum transverse-field term, H_1 and resums "analytically" all the terms in βH_0 and retains only the leading $(\beta H_1)^2$ term when evaluating thermodynamic averages.

[56] G. Mennenga, L. J. de Jongh, and W. J. Huiskamp, J. Magn. Magn. Mater. **44**, 59 (1984).

[57] P. Beauvillain, J. P. Renard, I. Laursen, and P. J. Walker, Phys. Rev. B **18**, 3360 (1978).

[58] In $LiHoF_4$ the value of the energy gap Δ between the ground-state doublet and the excited state for $B_x=0$ strongly depends on the crystal-field Hamiltonian. Since there is an ambiguity in the crystal-field parameters among different experimental works, there is also an ambiguity in the calculated energy gap. For different estimations of Δ see Refs. 16, 17, and 43.

[59] J. Magariño, J. Tuchendler, P. Beauvillain, and I. Laursen, Phys. Rev. B **21**, 18 (1980).

[60] L. M. Holmes, J. Als-Nielsen, and H. J. Guggenheim, Phys. Rev. B **12**, 180 (1975).

[61] We follow closely the method laid out in Ref. 62 as well as adopt their notation. However, we provide somewhat more details to assist the reader.

[62] R. J. Creswick, H. A. Farach, J. M. Knight, and C. P. Poole, Jr., Phys. Rev. B **38**, 4712 (1988).

[63] M. Le Bellac, *Quantum and Statistical Field Theory* (Oxford University Press, New York, 1992).

[64] M. Suzuki, Prog. Theor. Phys. **46**, 1337 (1971); *Quantum Monte Carlo Methods*, edited by M. Suzuki (Springer-Verlag, Heidelberg, 1987).

[65] H. Rieger and N. Kawashima, Eur. Phys. J. B **9**, 233 (1999).

[66] A. H. Cooke, D. A. Jones, J. F. A. Silva, and M. R. Wells, J. Phys. C **8**, 4083 (1975).

[67] J. E. Battison, A. Kasten, M. J. M. Leask, J. B. Lowry, and B. M. Wanklyn, J. Phys. C **8**, 4089 (1975).

[68] J. D. Jackson, *Classical Electrodynamics*, 3rd ed. (Wiley, New York, 1998).

[69] The magnetic permeability μ' is usually not known beforehand. In general as discussed in Ref. 51 it can be estimated rigorously in a self-consistent way. In the problem that we are interested in, we simulate an isolated sphere where the effect of the infinite continuum surrounding is incorporated via B_z^{sph} defined in Eq. (27). We are interested in the situation where $\chi_{\mathrm{sph}}=3/4\pi$. When this situation is fulfilled, the long needle-shaped bulk is in the paramagnetic regime, where in the thermodynamic limit the macroscopic magnetization of the infinite bulk is zero. Therefore, it seems quite reasonable to consider $\mu'=1$ for the infinite continuum without embarking in lengthy self-consistent calculations which are beyond the scope of this paper. Furthermore, this would appear *a posteriori* justified given that the simulation results are consistent with the simulation results obtained for a long needle-shaped bulk.

[70] H. J. Xu, B. Bergersen, and Z. Racz, J. Phys.: Condens. Matter **4**, 2035 (1992).

[71] I. I. Tupizin and I. V. Abarenkov, Phys. Status Solidi B **82**, 99 (1977).

[72] K. Binder, Z. Phys. B: Condens. Matter **43**, 119 (1981).

[73] A. I. Larkin and D. E. Khmel'nitskiĭ, Sov. Phys. JETP **29**, 1123 (1969).

[74] P. Stasiak and M. J. P. Gingras, arXiv:0809.0059, Phys. Rev. B (to be published).

[75] M. T. Hutchings, Solid State Phys. **16**, 227 (1964).

[76] K. W. H. Stevens, Proc. Phys. Soc., London, Sect. A **65**, 209 (1952).